

Microfluidic cells as a model 2D granular material

DISSERTATION ZUR ERLANGUNG DES
MATHEMATISCH-NATURWISSENSCHAFTLICHEN
DOKTORGRADES
"DOCTOR RERUM NATURALIUM"

IM PROMOTIONSPROGRAMM PROPHYS DER
GEORG-AUGUST UNIVERSITY SCHOOL OF SCIENCE
(GAUSS)

VORGELEGT VON:

Paolo Fantinel
aus Vittorio Veneto

Göttingen March 17, 2017

Betreuungsausschuss

PD LUCAS GOEHRING, *department of Dynamics of complex fluids, Max Planck
Institute for Dynamics and Self-Organization*

PROF. DR. STEPHAN HERMINGHAUS, *department of Dynamics of complex fluids, Max
Planck Institute for Dynamics and Self-Organization*

PROF. DR. ANDREAS TILGNER, *Institut für Geophysik, Georg-August-Universität*

Mitglieder der Prüfungskommission

PD LUCAS GOEHRING, *department of Dynamics of complex fluids, Max Planck
Institute for Dynamics and Self-Organization*

PROF. DR. ANDREAS TILGNER, *Institut für Geophysik, Georg-August-Universität*

Weitere Mitglieder der Prüfungskommission

PROF. DR. RALF SEEMANN, *geometry of fluid interfaces, Universität des Saarlandes*

PROF. DR. RER. NAT. DR.-ING. HABIL. ANDREAS DILLMANN, *Institut für
Aerodynamik und Strömungstechnik, Deutsches Zentrum für Luft- und Raumfahrt
(DLR)*

PROF. DR. CYNTHIA VOLKERT, *Institute of Materials , Georg-August-Universität*

PROF. DR. ANNETTE ZIPPELIUS, *Institute for Theoretical Physics,
Georg-August-Universität*

Tag der mündlichen Prüfung:

Contents

- Introduction** **1**

- 1 Materials and methods** **9**
 - 1.1 Microfabrication 9
 - 1.1.1 Photolithography 10
 - 1.1.2 Soft lithography 11
 - 1.2 Sample fabrication 12
 - 1.2.1 Drying samples manufacturing 12
 - 1.2.2 Drying sample design 15
 - 1.2.3 Displacement experiments 15
 - 1.2.4 Displacement sample design 16
 - 1.3 Setup and image analysis 18
 - 1.3.1 Experimental setup 18
 - 1.3.2 Image analysis 20
 - 1.4 Scaling 21
 - 1.5 Minkowski functionals 23

- 2 Models** **27**
 - 2.1 Drying model 27

Contents

2.2 Displacement model	30
3 Results	35
3.1 Drying	35
3.1.1 Reproducibility control	36
3.1.2 Uniformly distributed random disorder	40
3.1.3 Normally distributed correlated disorder	42
3.1.4 Diffusion versus Invasion	49
3.1.5 Wettability	50
3.1.6 Salt	50
3.2 Immiscible fluid-fluid displacement	52
4 Discussion	57
4.1 Drying experiments	57
4.1.1 Absolute initial drying rates	58
4.1.2 Disorder effects	58
4.2 Displacement experiments	59
Acknowledgements	63

Contents

Introduction

Two-phase flow processes in porous media are a broad research topic with implications in several engineering fields such as transfer of pollution in the vadose zone [1], mobilization and recovery of hydrocarbons [2, 3], and CO₂ sequestration [4]. Being able to predict patterns, phase distributions and transfer rates during two-phase flow in porous media is crucial in processes where the fluid phase interacts directly with the porous material, such as deposition of salt [5, 6] and aquifer and soil remediation processes [7]. Such processes are complicated to study as they involve interactions between different physical mechanisms and time- and length-scales [8, 9]. Drying of porous materials and immiscible fluid-fluid displacement are important examples of two-phase flow process which occur in both natural and engineered systems [10]. These phenomena are studied experimentally in this thesis and compared to models developed by my collaborators at the Hebrew University of Jerusalem in Rehovot, Israel.

Drying is a fundamental process in soil-atmosphere energy and moisture exchange [11] and in solute transport within soils [5] and in agriculture [12]. Drying of porous media can be approached as an immiscible displacement where an invading fluid penetrates the medium by displacing a more viscous defending fluid as the latter evaporates [13]. During drying, long periods of evaporation from a static air-liquid interface are interrupted by sudden invasion events called "Haines jumps" [14, 15]. When such jumps, or bursts,

Contents

occur, pore-scale, air-liquid interfaces connecting adjacent solid particles depin and reach the next stable position, inducing liquid flows that cause interfaces at other locations of the liquid bulk to readjust on a very short timescale [9, 15]. Drying in porous materials can be separated into two different stages based on their characteristic drying rates and transport mechanisms. During the first stage, liquid is transported, mostly via flow from the bulk through connected liquid pathways, to the medium's surface where evaporation occurs [16]. During this stage, evaporation rate is fairly constant (constant rate period) and influenced mostly from surface wetness, size distribution of surface pores and surface boundary conditions [17, 18, 19]. Stage two is identified with the loss of connectivity between the surface and the liquid bulk. In this stage, vapor diffusion within the medium becomes the dominant transport mechanism [20, 21] causing the drying rate to drop visibly (falling rate period) due to the longer characteristic time scales of diffusion as opposed to liquid flow.

Another important two-phase flow process in porous media is immiscible fluid-fluid displacement. This is a relevant process in many natural and industrial process such as oil recovery [22], CO₂ geosequestration [23], groundwater contamination [24], soil wetting, drying and dyeing of paper and textiles. The mechanisms governing fluid displacement are quenched disorder [25], short-range cooperative effects and long range pressure screening [26]. These depend on a large numbers of parameters including the wettability of the porous medium [26, 27]. As a consequence, the patterns arising during displacement range from a stable, compact front to a ramified pattern with preferential flow paths (fingers)[28]. Depending on the length-scales and the displacement velocity at play, viscous or capillary forces dominate the formation of patterns determining formation of viscous or capillary fingers. Fluid invasion is a phenomenon similar to many problems

characterized by competitive domain growth and nonlinear interface dynamics, including magnetic domains, biological films and flame front propagation [29]. The evolution of interfaces in these phenomena is often modeled as a competition between phases and constraints arising from disorder. The relative importance of these factors can be set by tuning properties such as wettability in fluid displacement [26, 27] or local random interaction fields in magnetic domains [30]. Understanding the impact of wettability would therefore be relevant to a wide range of phenomena of technological importance. Disorder in pore sizes is a factor in media such as soils and rocks [31] and even in engineered devices due to the limited fabrication resolution [32]. In some industrial applications low disorder is desirable [33] as homogeneous fluid distribution and control over the patterns are needed. Preferential pathways and heterogeneous fluid distributions in the patterns, dictated by disordered media, can be an advantage in applications where fluid mixing and reactions [7, 34] are needed, while they may be a disadvantage when efficient sweep of hydrocarbons [35] or contaminants [7] are needed.

The effects of disorder on invasion patterns at capillary or viscous regimes is generally accepted. For slow drainage, where a wetting fluid is displaced, high disorder was shown to promote trapping promoting the transition from compact patterns to viscous fingering in both experiments and simulations [36, 37, 38, 39, 40, 41, 42]. For slow imbibition, where the defending fluid is nonwetting, simulations show a transition from compact to faceted growth as disorder is decreased (capillary fingering) [38, 43]. Ordered faceted patterns were observed as well for imbibition at uniform pore sizes at favorable viscosity ratios (i.e. when the defending fluid is less viscous than the invading fluid). At the other end of the spectrum, for fast displacement, decreasing disorder promoted viscous fingering [40, 44] with fewer straighter fingers. At intermediate displacement velocities both viscous and

Contents

capillary forces play an important role in the displacement and, qualitatively lowering disorder enhances the displacement efficiency [36, 39, 40, 41, 42]

Computationally, a three dimensional porous system is a difficult task, although attempts have been made in this direction [15], due to a limited numerical resolution arising when dealing with such a high number of variables [45]. A possible solution is to approach the problem from a two-dimensional description and, once the main features are captured, expand to a three-dimensional approach. Pore-network models (PNM) originally proposed in [47] have become accepted in modeling multi-phase flow in porous media [48] thanks to their combination of computational efficiency and the ability to capture pore-scale physics. In general, PNMs schematize porous media as a collection of pores communicating through restrictions (or throats) and they are based on balancing flows of liquid and vapor masses in the pores. Transport properties commonly included in these models are vapor transfer (both diffusive and convective) and viscous liquid flows [49]. Depending on the level of complexity desired, PNMs can include the shape of solid particles in the pore-medium in order to include, for example, wettability effects [26, 25]

First applications to drying were made in [50, 51] and were able to calculate effective permeabilities [51] and the stabilizing effects of gravity on the invasion front [50]. Generally, PNMs are based on mass balance of liquid and vapor in single pores and transport can occur through diffusion and convection of vapor and viscous liquid flow [49]. PNMs have also shown the effects of capillary pumping [52] on invasion patterns and liquid flow through films in the corners of angular pores on drying rates [53]. In [54] a model is proposed where the porous medium is coupled with its external, diffusive, boundary layer allowing solution of complex boundary layer conditions and processes.

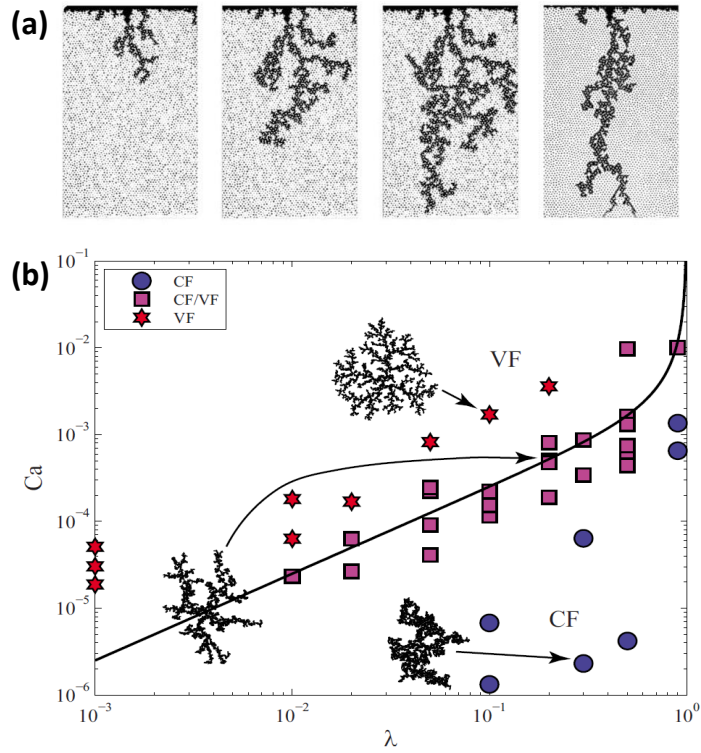


Figure 0.1: I show examples of patterns forming during drying (a) (reproduced from [45]) and immiscible fluid displacement (b) (reproduced from [46]). I show a phase plot of the fingering patterns that form, depending on the dominance of capillary or viscous forces during the displacement, for various amounts of heterogeneity in the pore-space.

Contents

In fluid-fluid displacement phenomena, drainage has been studied more thoroughly, identifying different invasion behaviors and explaining their dependence on the flow velocity, fluid viscosities, interfacial tension and the degree of pore scale disorder [40, 39, 55, 56]. Decreasing the wettability of the defending fluid was found to stabilize the displacement and reduce trapping in forced and gravity driven drainage experiments [57, 58]. However, relatively few works have studied imbibition and they have done so focusing mostly on the stable case of a more viscous invading fluid [56, 39, 59]. For unstable viscosity ratios (where the invading fluid is less viscous), experiments showed a marked difference between viscous fingering in drainage and more stable patterns with thicker fingers in imbibition [60]. Stabilization was captured in simulations which used stochastic viscous effects [61] and in Lattice Boltzmann simulations [62]. Quasistatic simulations illustrated that decreasing the wettability of the defending fluid stabilized displacement, leading to a compact front in slow imbibition regardless of the unfavorable viscosity ratio [63].

On the experimental front, transport in porous media has been studied in different ways including etched channel networks [64, 54, 65], Hele-Shaw cells containing cylindrical pillars [45, 66] and monolayers of glass beads [13, 67]. All of these experiments have focused on long throat networks [64, 54, 65], length-scales that are not comparable with those of real soils [45, 68] or small pore networks [69] removing manufacturing problems related to working with micron-sized objects. In this thesis I aim to connect pore-scale observations of drying phenomena to their macroscopic interpretation by testing a class of two-dimensional, minimal models and comparing them to two-dimensional experiments.

The inspiration for the experiments presented in this paper comes from microfluidics, the science and technology of systems that manipulate small amounts (10^{-9} to 10^{-18}

liters) amounts of fluids using channels with dimensions of tens to hundreds of micrometers [70]. This field has four parents: molecular analysis, biodefence, molecular biology and microelectronics [70]. First, the development of gas-phase chromatography, high-pressure liquid chromatography and capillary electrophoresis combined with the use of lasers in optical detection made it possible to achieve high sensitivity and resolution using very small amounts of samples. The risk of chemical and biological weapons being employed in military and terrorist attacks [70], the need of highly sensitive, high-throughput and high-resolution analytical methods in genomics [70] made it necessary to develop portable and highly efficient devices. Finally, microelectronics gave the fabrication methods constituting the base of microfabrication techniques used in microfluidics today [70]. The success of silicon microelectronics gave the hope that microfluidics could be a direct translation of this field and, at the earliest days, some microfluidic chips were actually realized using silicon and glass. However, for analysis of biological samples these materials are usually inappropriate as they lack the gas permeability needed to work with organic samples. Furthermore silicon is expensive and opaque, making it inappropriate for the conventional optical detection methods. The most widespread material in microfluidics today is poly(dimethylsiloxane)–or PDMS– thanks to its completely different properties from those of silicon [71, 72]. PDMS is transparent, permeable to gases, non-toxic and elastic, making it ideal for biological applications. PDMS is also inexpensive compared to silicon and easy to use, making the production times of samples much shorter when compared to chips using glass or silicon. Soft lithography [73] in particular is a class of microfabrication techniques that allows to reproduce a pattern from a mold, or master (typically produced via photolithographic techniques [74]), within hours when using PDMS. Other polymers are used in microfluidics, such as Norland Optical Adhesive, poly(methyl methacrylate) or other plastics and resins depending on the application

Contents

of the chips.

The crucial feature of microfluidic techniques for the purpose of this thesis is the ability of producing micron-scale objects of known, controllable size and position. It is possible to produce two-dimensional systems at a scale that is comparable to those relevant in geological and agricultural applications. Furthermore, unprecedented control over size and position of the pores is now achievable and the possibility to reproduce the experimental geometries exactly in the simulations allows for direct comparisons between experimental and simulated results.

In this thesis I present two types of experiments dealing with multiphase flow in granular materials. I use microfluidic cells to study drying and immiscible fluid-fluid displacement in two-dimensional porous systems. I start by illustrating the fabrication methods used to make the cells and the method used to extract the relevant variables in the first chapter. I will then summarize the models I have tested with my experiments in Chapter 2. In Chapter 3 I will present the experimental results and I will discuss them in Chapter 4. Finally I will summarize the thesis and discuss future directions for this project in Chapter 5.

1 Materials and methods

In this chapter I will illustrate the microfabrication and analysis methods used to obtain the results presented in this thesis. I will start by showing the microfabrication techniques and the sample designs. I will then proceed to describe the experimental setup and procedure, the processing of the experimental pictures and the metrics we used to characterize my results.

1.1 Microfabrication

Microfabrication techniques are used in several fields where it is necessary to produce micron-scale features such as microfluidics, microelectronics, fabrication of sensors, microreactors, combinatorial arrays, microelectromechanical systems (MEMS), microanalytical systems and micro-optical systems [70]. The word 'microfabrication' includes different techniques. A comprehensive review can be found in [74, 70]. For the purpose of this thesis I will present mainly two techniques: photo- and soft lithography. I present them in details in the next sections. I will then give details about the sample that were produced

1.1.1 Photolithography

Lithography (from greek *lithos*-, rock, *graphein*, writing) is a process that allows transferring of a pattern to a surface by means of an engraved mold. Lithography was, for example, the process that allowed the printing revolution in the XV century. Then, molds reproducing letters of the alphabet were used to print books at unprecedented rates. The technique has evolved and allowed development of techniques like microcontact printing [75] or photolithography [74].

Photolithography is a technique that allows transferring of a pattern to a photosensitive layer (photoresist or simply resist) by exposing it to light through an optical mask. A mask consists of a transparent support with opaque features reproducing the desired pattern [74]. When the features to be reproduced are larger than $\sim 10\mu m$ the mask can be made of a transparent acetate sheet where the features are laser printed. If a higher resolution is desired (down to $\sim 1\mu m$, the mask can be made of a transparent layer of quartz where the pattern is made of chrome or iron oxide. I will now illustrate the process. A schematics is shown in Fig. 1.1.1

The process usually starts with a silicon wafer onto which a photoresist is spin-coated. Glass or other materials can be also used as a substrate in case one wanted to etch it [74] exploiting its amorphous nature or otherwise use it in the final sample. Spin coating allows to spread a uniform layer of photoresist onto the substrate ranging from $\sim 1\mu m$ to $200\mu m$ depending on the resist used [76, 77, 78]. The coated wafer is then heated up on a hot plate for variable times, depending on the layer's thickness [77, 78] in order to promote crosslinking by initiating evaporation of the solvents that maintain it in a liquid state.

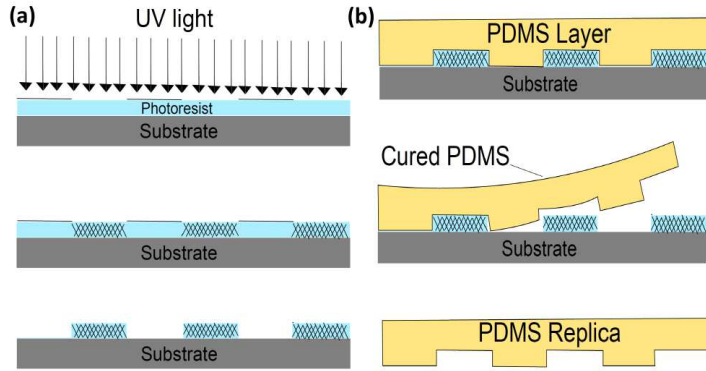


Figure 1.1: Schematics of the photolithographic and soft lithographic process. A solid substrate is spin coated with a photosensitive polymer, which is exposed to UV light through a mask reproducing the desired features. The exposed area crosslinks whereas the unexposed area remains liquid and can be removed using an appropriate solvent. Liquid PDMS is then poured on the substrate, cured thermally and later removed, providing the negative, transparent copy of the original master.

After the pre-bake step, the resist layer is placed in contact with the optical mask to limit diffraction effects and perpendicularly exposed to UV light of appropriate wavelength. A positive photoresist will crosslink in the unexposed areas while a negative resist will crosslink in the exposed areas. Negative photoresists allow production of thicker layers (up to $\sim 200\mu m$)[77], while positive resists do not allow structures thicker than $\sim 2\mu m$ [76]. After exposure, the substrate is baked again to further promote crosslinking before the sample is developed.

The sample may now be immersed in the appropriate solvent in order to remove the non-crosslinked areas and leave the desired pattern on the substrate. In order to promote developing in the corners of the sample and in smaller features, the container is shaken occasionally. The final sample could now be used for etching or as a mold for replica molding [74], a process that I will illustrate in the next section.

1.1.2 Soft lithography

Soft lithography is a technique that allows reproducing the negative of some pre-existing pattern. It works at virtually every scale ranging from micron sized objects, such as those I describe in this thesis, to macroscopic ones, such as cakes or concrete walls.

The basic procedure involves pouring a liquid onto mold and than solidify it through heat or light exposure. If we take a sample produced with photolithography as a mold and we pour a liquid elastomer, usually poly-dimethylsiloxane (PDMS), on the structure, the elastomer will take the negative shape. PDMS can be cured through heat and its elasticity allows us to easily detach it from the mold without breaking it or bending the replica permanently. This process is called replica molding and allows to rapidly produce a negative of any structure [72] which can later be used as a microfluidic chip or as mold itself in order to obtain an elastic, positive copy of the original sample. Other polymers can be used to make a replica, however, in order to detach them from the rigid substrate, elasticity is crucial to preserve the shape of the replica and the integrity of the master which could otherwise break.

Photo- and soft lithography were the core of the microfabrication process. I will now explain in detail how I made the samples used in this thesis.

1.2 Sample fabrication

In this section I will describe how the specific samples were produced. Although different sets of samples were produced for different kinds of experiments, the techniques are very similar and I will only highlight the differences between samples made for the specific experiments.

1.2.1 Drying samples manufacturing

The sample for our drying experiments used a photolithographic step followed by several replicas. The final chip was made of Norland Optical Adhesive 81, NOA, a photosensitive glue. Here I give a detailed description of the steps taken to produce the samples. The sample design as well as an example of the final product are shown in Fig.1.1.

One starts by spin-coating a negative photoresist (SU8 3025, MicroChem Corp.) onto a silicon wafer to obtain a flat layer of thickness $40\ \mu\text{m}$. The sample is pre-baked for 1 minute at 65°C and for 15 minutes at 95°C . It is successively allowed to cool down before the exposure to UV light. The sample is exposed to UV light (wavelength $362\ \text{nm}$) through an acetate mask reproducing the desired pattern until an energy of $200\ \text{mJ}/\text{cm}^2$ has been transferred from the UV lamp to the resist (the length of the exposure depends on the lamp used, for our lamp the exposure lasted about 30 s). SU8 is a negative resist, therefore areas exposed to light crosslink and the unexposed areas remain in a fluid state. The sample is then baked again for 1 minute at 65°C and for 5 minutes at 95°C . Again, I let the sample cool down before I place it in a Petri dish and pour the developer (mrDev 600) onto it. The Petri dish is agitated now and then to promote removal of the liquid photoresist in the smaller features. I take the sample out of the resist every few minutes, dry it with a nitrogen jet and rinse it with isopropanol. When the dried sample does not show interference fringes due to residual films of SU8 or white residuals of isopropanol after being dried it is ready to be used as a mold for the replica step.

PDMS needs to be mixed with a catalyst in order for us to cure it after it is poured on the mold. Mixing the catalyst (in a ratio of 1:10) by stirring produces many bubbles in the mixtures. Due to the viscosity of liquid PDMS, waiting until the bubbles disappear would cause the PDMS to cure before it can be used. Therefore these bubbles are

1 Materials and methods

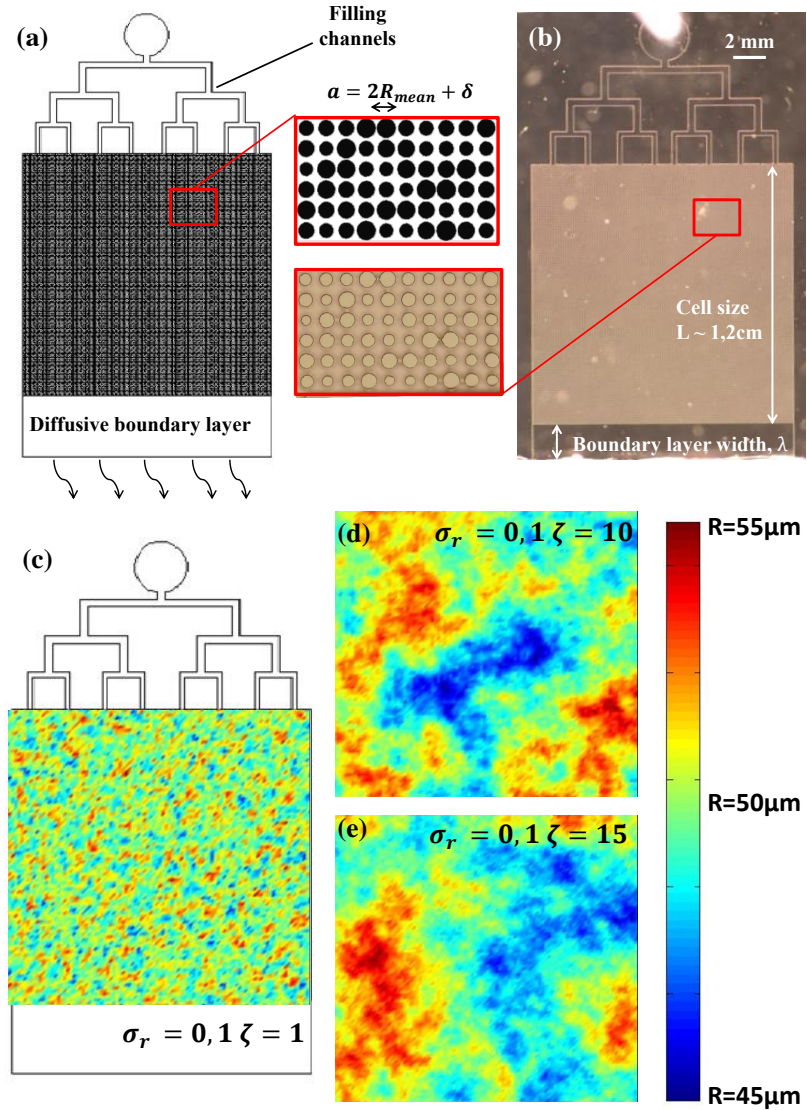


Figure 1.2: From design to fabricated sample. The mask design (a) shows how a chip is conceived, with an inlet splitting into several channels that allow for a uniform filling of a square pore space. The actual sample (b) reproduces the design and the boundary layer, across which evaporation occurs, is cut to the desired width. The insets show a direct comparison of the designed and realized features in the pore space. I show the concept behind correlated disorder (c) where the color code represents the pore-size distribution, red corresponding to small pores, green to intermediate and blue to large pores. The color map shows a sample with correlation length $\zeta=1$. I also show samples with $\zeta=10$ (d) and $\zeta=15$ (e)

1.2 Sample fabrication

removed by placing the mixture under vacuum until no bubbles are visible. Liquid PDMS is poured onto the mold and the sample is placed under vacuum again in order to remove bubbles that may form between the pattern and the elastomer. These bubbles would ruin the replica, not allowing production of a precise negative of the structure and hindering optimal imaging of the experiment. I then cure the PDMS for one hour in an oven at 75°C. The cured PDMS layer is peeled from the master and I use it as a mold for a further PDMS copy. In order to do this, I have to first treat the PDMS mold so that its copy can be removed. The treatment consists in exposing the mold to a plasma for 2 minutes and then put it in contact with a 5% solution of Poly(diallyldimethylammonium chloride) (PDADMAC) for 40 minutes. This step changes the wettability of the PDMS [79]. In my case, after all the bubbles are removed again and the elastomer replica is cured, it allows me to detach its PDMS negative. I now have a copy of the original SU8 sample and use it as third mold to make a NOA replica.

Before I explain this final replica step, I would like to point out that the choice of NOA as a material for my samples was dictated by its impermeability to the oil I use in my experiments. The same does not apply for PDMS which is permeable. A NOA replica from the SU8 sample would not be possible, as cured NOA is rigid and detaching it from a rigid mold would be very complicated as the process could break the mold, the smallest replicated features or permanently bend the NOA negative. Also, skipping one PDMS replica by taking the negative of our final design as a starting point in the SU8 mold was not an option. Referring to Fig. 1.1, we see in the inset how the circles on my masks are opaque. In principle, the opposite polarity, with transparent circles on an opaque background, would allow me to limit the fabrication to one PDMS replica and, finally, a NOA sample. However, due to diffraction effects during the exposure, transparent circles

1 Materials and methods

on the mask visibly produce much smaller structures than I design. Therefore I chose the procedure I have illustrated.

A base for the chip is prepared by coating an acetate sheet with NOA. I initiate the curing of the two parts of my chip by exposing them to UV light for about 10 seconds. Once cured, the NOA layer is removed from the PDMS mold. Both components are then placed in a plasma cleaner for one minute. This primes their surfaces so that they are able to adhere to each other. Finally, body and base of the chip are pressed together. The base sheet can deform slightly during this step, especially around areas free of microfluidic structures, such as pillars. However, having such a flexible component in the chip is necessary to guarantee uniform bonding throughout the sample. The bonded chip is then exposed to UV light for 10 minutes in order to complete curing. Freshly cured NOA is yellow, but its color is lost after exposure to white light. Thus, after fabrication I expose the chip to white light for about 24 hours in order to stabilize its color for image analysis. This also stabilizes its wettability [80].

1.2.2 Drying sample design

After fabrication, the samples are thin square cells with an open boundary layer on one side to allow evaporation, as can be seen in Fig. 1.1. I usually fix this layer to be $\lambda = 2$ mm wide. However, to test the effects of different boundary layers on drying (e.g. [17]), it could be varied between 0.5 and 4 mm. On the opposite side of the chip I designed an inlet that successively split into eight channels. I use these to fill the cells uniformly with a perfectly wetting (contact angle $\simeq 3^\circ$) volatile oil or water. A 2D porous material is then realized by having an extensive array of round pillars in the cell. I can vary the sizes and positions of the pillars to mimic heterogeneous random packings, as would occur in

1.2 Sample fabrication

a real soil. Using the soft lithography techniques described above, a minimum feature size of $5 \mu\text{m}$ and a feature resolution of $2 \mu\text{m}$ can be achieved. To simplify comparison to numerical modelling I designed my samples as an array of pillars lying on a square grid. Other designs, such as a random close packing or a triangular lattice, could just as easily be manufactured to match models like those in Refs.[37, 26].

I introduce heterogeneity into the design by setting a window within which the radii of individual pillars can vary within a given distribution. For example, the radius of each pillar could be randomly selected within the range of $45\text{-}55 \mu\text{m}$ (i.e. a uniform distribution with a relative width of 10%). Radii heterogeneity is not, however, the only parameter I tuned. In some samples I also introduced a correlation length to the radius distribution, to increase the probability of having similar-sized pillars group together. The sizes of the pillars in these locally correlated samples correspond to the relative heights of a random rough surface at their locations. Such surfaces were constructed by summing ten thousand sine waves with random phase and wave number selected randomly from a Gaussian distribution. The width of this distribution, in Fourier space, is inversely proportional to the correlation length of the pillars in the final design. The radius distribution is now also Gaussian, and could be scaled to give as broad or narrow a distribution as desired. Furthermore, the distribution is clipped by setting a maximum radius and grid spacing in the samples in order to avoid pillar overlaps that would close a pore/throat and would be complicated to model.

Therefore I present two types of drying experiments (Fig.1.1: one where the cells have no correlation length (or $\zeta = 0$) and the pillar radii heterogeneity within any one sample are randomly taken from a uniform distribution with a relative width of $\sigma_r = 3, 5, 10$ or 20% ; the other has Gaussian distribution of radii with a width $\sigma_r = 10$ or 20% and

1 Materials and methods

correlation lengths $\zeta = 1, 4, 10$ or 15 pores. Samples have a thickness of $40 \mu\text{m}$, and contain a 100×100 grid of pillars with an average pillar radius of $R = 50 \mu\text{m}$ and average throat size of $\delta = 25 \mu\text{m}$ (and hence a grid spacing $a = 125 \mu\text{m}$). Using these parameters I also avoid any overlap of pillars and maintain a minimum throat size of at least $5 \mu\text{m}$. These designs give square cells of size $L \sim 1.2 \text{ cm}$.

1.2.3 Displacement experiments

The samples I used in displacement experiments were made using the same techniques explained so far. I used SU8-100 to spin-coat the silicon wafer and obtain a layer of $60 \mu\text{m}$ thickness as prescribed by the manufacturer [77]. Pre- and postbake times as well as the exposure time were adjusted according to [77]. Because I was looking for a hydrophobic material, I have used PDMS as the material for my final chips. Therefore I was able to limit the replica steps to one, by otherwise using the same procedure illustrated in this section. The substrate to close the chip is now PDMS as well. To bond the two parts of the chips, I placed them in a plasma cleaner for 30 s. This primes the surfaces to adhere to each other allowing one to close the chips by placing the two parts in contact.

Exposure to plasma temporarily increases the wettability of PDMS [81]. To revert it to its original state, I place the sample in an oven at 75°C for ~ 45 minutes.

In order to avoid leaks at the inlets during the experiments, I plug the tubes in the PDMS sample, cover it with NOA81 and cure it. Placing a drop of NOA on the inlets would make the image analysis more difficult, changing the index of refraction in the areas covered. Therefore I cover all of the sample's surface in order to have a uniform background. This guarantees the absence of leaks, allowing us to perform the experiments in the way I describe in section 1.3.

I will now describe the displacement samples in detail, showing the symmetry of the pore-space and design of the cells precisely.

1.2.4 Displacement sample design

Displacement samples have a similar design as the drying ones. I show a sample geometry in Fig.1.2. We now have a circular geometry, with an inlet in the center and two outlets at opposite poles. I leave a 1 mm boundary between the pore space and the outlets to keep a uniform pressure around the cell until the invasion front reaches the end of the pore-space (breakthrough). The granular material is again made of pillars, although they now lie on a triangular, equilateral grid with side $a = 180\mu\text{m}$ in order to allow more pore-invasion mechanisms (see section 2.2). The pillars have, on average, a $60\mu\text{m}$ radius and a $60\mu\text{m}$ average throat size. Heterogeneity is set again within a uniform distribution. Pillars in different samples are now stretched in order to maintain the same relative disorder with the same relative throat- and pore-size distribution in order to minimize effects due to random geometrical variations, except for one sample where I re-randomized the pillar sizes.

I therefore present three cells with the same relative disorder and heterogeneity $\sigma_r = 3$, 20 and 37% of the average radius and one further realization of a cell with a 20% heterogeneity. The cells are now made with PDMS as I want the defending fluid to be non-wetting in order to study imbibition.

1.3 Setup and image analysis

I will now describe the experimental setup and the way I have treated experimental pictures in order to analyze them.

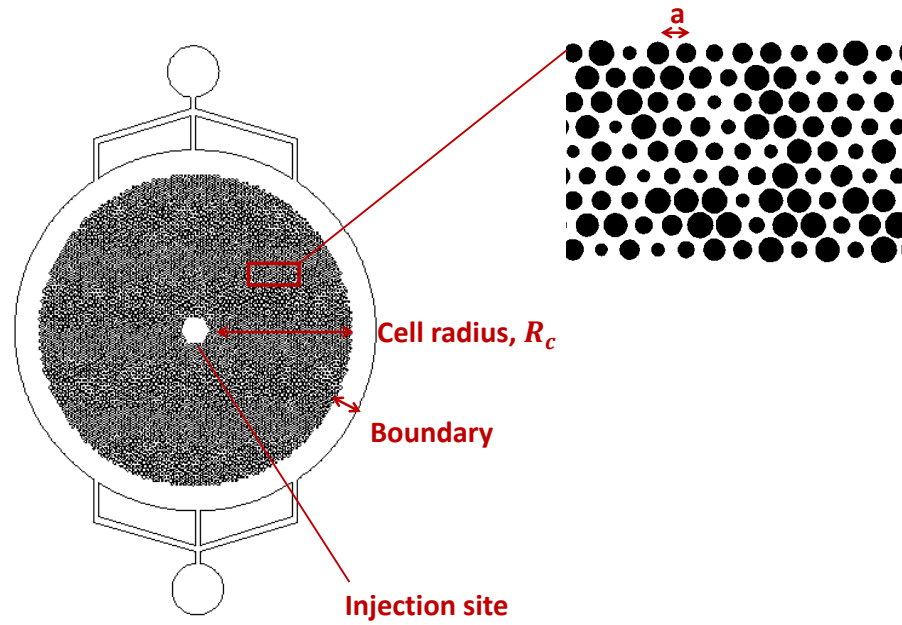


Figure 1.3: I show the sample design of our fluid-fluid displacement experiments. A round cell containing pillars on a triangular grid is manufactured leaving the space for the inlet in the middle. I enforce constant pressure at the boundary by leaving a 1 mm boundary layer around the cell where fluid can flow with a minimal pressure drop compared to the porous medium. This is connected to two outlets to allow the displaced fluid an escape path from the cell.

1.3.1 Experimental setup

The setup is virtually the same in both drying and displacement experiments, therefore I will give a general description and only briefly mention the minor changes done between the experiments.

In order to observe my experiments I put a cell under a Nikon DSLR 7500 camera equipped with a macro lens that allows for time-lapse digital imaging with a pixel resolution of $5\ \mu\text{m}$ and a time resolution of 1s . The sample was left horizontal in order to avoid gravitational effects on the drying process. The chip is surrounded laterally by a ring of LEDs. Having light from the sides allows the camera to essentially only see light scattered from interfaces, in a technique similar to dark-field microscopy. The wet area therefore appears darker than the dry area as the refractive index of the liquids I have used in the various experiments is higher than that of air and closer to that of the material of the microfluidic cell. By darkening all other sources of light in the room, I also ensure that there are no reflections on the top of the cell that might interfere with image analysis.

In drying experiments I want to have evaporation only from the open boundary. To ensure this, I fill the cell with Novec 7500 –a volatile fluorinated oil– using a syringe connected to the cell’s inlet through a tube. I remove the tube from the inlet, spread some high vacuum grease (Dow Corning) on the hole and press a piece of NOA on it. This leaves the boundary layer as the only place for the oil to evaporate.

In displacement experiments, having an inlet in the middle of the cell prevents the camera from taking a clean picture of what happens inside the cell from above because the tube connecting it to the syringe would be between the cell and the lens. Therefore

1 Materials and methods

I make a slightly raised support for the cell. This allows me to flip the sample, so the tubes are under the cell and I can observe the experiment from the opposite side of the sample compared to the inlet, making image analysis easier. I fill the microfluidic chip with water or water–glycerol mixtures, as glycerol mixes well with water and allows to make a mixture with higher viscosity depending on its fraction. Tuning the viscosity of the liquid allows me to increase the capillary number in the injection process. Since water does not wet PDMS very much (Typical contact angle 108°), I need to be particularly careful when filling the cells, as there may be some bubbles in the porous medium that would introduce a bias in the experiments. Most of the times however, I am able to flush these bubbles out of the sample through the outlets. Once the cell is full, I change the syringe with one filled with air and use a syringe pump that allows injection speeds of up to 1.74×10^{-2} mm/s. Depending on the water–glycerol mixture I use and on the syringe I use to inject the air, I can achieve capillary numbers $Ca \sim 10^{-6} - 10^{-3}$.

The experiments take place while the camera takes a picture periodically. The maximum frequency allowed by the camera is 1 picture per second. It is much more than I need for drying experiments, that usually last ~ 1 hour, while it is a little coarse for displacement experiments, that take ~ 10 seconds. The time lapse sequence continues until the leading front of the air–liquid interface reaches breakthrough, that is, when the invasion front reaches the filling channels in the drying experiments and when it reaches the outer border of the pore space in the displacement experiments, as this disrupts the pattern.

The images are finally processed using Matlab in order to extract quantities for our analysis. I explain the procedure in the next section.

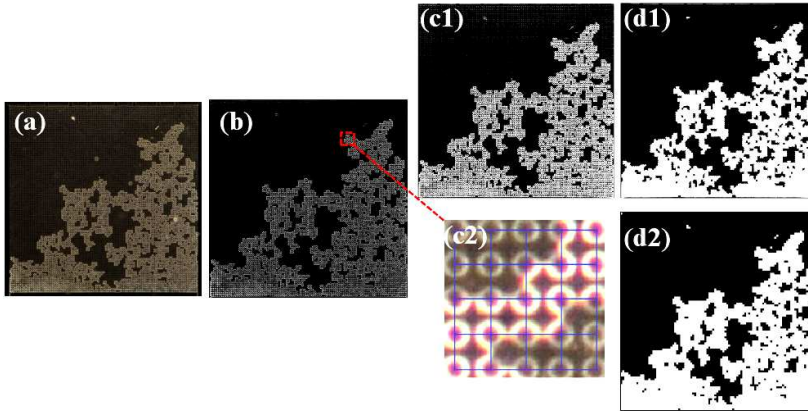


Figure 1.4: Image analysis. I start from a color picture (a) which I flatten into a greyscale image and then apply a band pass filter to eliminate both noise and intensity variations. Further subtracting constant sources of noise gives us a cleaned image (b). This can be either thresholded (c1) and transformed using morphological operations to produce a continuous black-and-white picture of the drying pattern (d1) or it can be discretized using its mask design and the intensity in each pore (c2) in order to show which specific pores are open at the given time (d2).

1.3.2 Image analysis

The image analysis procedure is very similar in both sets of experiments. The experimental images are processed with Matlab in order to compute quantities such as the liquid saturation, the number of isolated liquid clusters and the shape of the air-liquid interface at every point in time during drying. In order to extract such quantities the experimental pictures have to be converted into a binary form. An example of the process is shown in Fig. 1.3.2.

I start by extracting the red color channel of the image, which contains the best contrast. To this I then apply a bandpass filter to remove both the high-frequency noise (cutoff: 3 pixels) and any low frequency variations in intensity (cutoff: 30 pixels). From

1 Materials and methods

each image I also subtract the first picture in its sequence in order to remove constant sources of background noise, such as dust or flaws in the microfabricated chips. The cleaned picture (Fig.1.3.2b) is then thresholded to give a binary image (Fig 1.3.2c1), that distinguishes between wet (black) and dry (white) areas. Next, I remove any white objects smaller than a pore size (about 100 pixels), such as wet pillars, which might still be partially visible in the binary image, in order to leave the wet area completely black. I then dilate the remaining white objects, affecting the contour of the dry pillars and the air-liquid interface, and remove the isolated black regions corresponding to pillars in the dry areas. Finally, I erode the picture to reverse the dilation and to give a map of the wet and dry regions where all the pillars have been removed. The accuracy of these image processing steps was monitored, and they were adjusted slightly, to prevent the loss of fine detail in any particular image sequence.

In order to exploit the precise knowledge of the geometry of my samples and make comparisons with the model, I also employed a second stream of image processing (developed by Wieland Lüder in his bachelor's dissertation [82]), which summarizes the entire image sequence in a discrete matrix form. This is a 99×99 matrix, $T_{i,j}$, where each element specifies the time at which air first invades the corresponding pore, at location (i, j) . The process used to extract these matrices was developed by Wieland Lühder in his bachelor's dissertation [82]

To extract this matrix from the data, I start from the cleaned greyscale picture mentioned above (Fig. 1.3.2b). From this I manually find the pixel coordinates of the pores at opposite corners of the cell, corresponding to locations $(1,1)$, and $(99,99)$. These are then used to scale the mask design to the size of our images and thus to map all pillar coordinates. A pore is then defined as the open space between the centers of its adjacent four pillars. When looking at the area of the image that is around a single pore, there are

four quarter-pillar crowns visible at its corners. I consider a pore dry when these crowns are dry. For any pore all four quarter-pillars were either dry or wet at the same time, as a partially filled pore was neither observed experimentally nor is allowed for in the model. A dry pore shows brighter crowns at the corners than a wet pore, as an air-NOA interface scatters light more than an oil-NOA interface does. I exploit this difference to choose an intensity threshold below which the pore will be considered wet. By analyzing the time-lapse sequence, I am thus able to determine the first time at which any particular pore (i,j) is observed to be dry. The pore invasion matrix, $T_{i,j}$, records these times, and is demonstrated in Fig.1.3.2d.2.

1.4 Scaling

In order to simplify the description of my experiments and to ease comparison with the numerical pore-network model, I non-dimensionalize all variables. To do so, I first notice that the drying rate is constant in the early stages of my experiments. Therefore, I find the drying rate by computing a numerical derivative:

$$\dot{e} = \frac{1}{L} \frac{\Delta A}{\Delta t} \quad (1.1)$$

where ΔA is the increase in dry area from one picture in the sequence to the next, Δt is the time interval between the two pictures and L is the length of the side of the cell. The initial drying rate, e_0 , is taken to be the slope of a linear fit of the evaporation rate data over the first 40 minutes of any experiment. Since e_0 is constant, within the experimental sensitivity, I use it to scale \dot{e} and obtain a nondimensional drying rate \dot{e}/e_0 .

In order to reduce the noise caused by taking a numerical derivative in the drying rate, I apply a 20th order low-pass filter to the raw data ($\Delta A/L\Delta t$) with frequency cutoff 0.1.

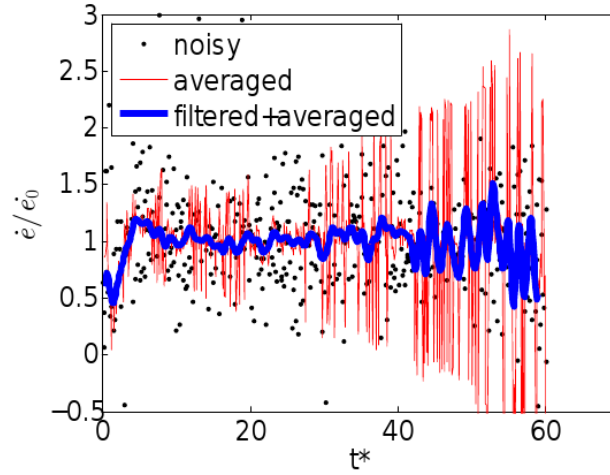


Figure 1.5: Smoothing process on a sample drying rate. I show the drying rate extracted from the picture sequence as black dots; the results of applying a 5-point mobile average to the raw data as a red line and the results of applying a low-pass filter and a 5-point mobile average as a blue line.

The filtered data is then averaged using a five-point mobile average to enhance smoothing of the data. I show the results in Fig. 1.3. There we can see how the filtering I apply considerably reduces the noise coming from the analysis of the raw pictures.

I now define a characteristic length-scale using the spacing between adjacent of pillars, a . For example, the side of our cells has length $L = 100a$, and so a dimensionless size of $L^* = 100$. The initial drying rate is then used to define a characteristic timescale, τ , as the time it takes to dry the first row of pores:

$$\tau = \frac{a}{|\dot{e}_0|} \rightarrow t^* = \frac{t}{\tau} \quad (1.2)$$

where \dot{e}_0 is the initial drying rate and a is the grid spacing of the pillars. If the drying rate was constant throughout the experiment, then $t^* = 100$ would be the dimensionless

time needed to dry the whole cell.

The scaling in the displacement experiments will be the same, where it applies. For example, I cannot compute a displacement rate (analogous to the drying-rate) because of the lack of time resolution of our camera ($\simeq 1s$) compared to the time scale of one experiment ($\simeq 10s$). I only compare patterns at breakthrough. At this point in the experiments I can still compute the metrics that characterize the patterns and I will introduce them in the next section. The patterns forming in immiscible fluid-fluid displacement are expected to depend on the geometry of the samples, i.e. the relative disorder, and on the injection speed. In order to nondimensionalize this speed, I use the Capillary number, defined as the ratio of viscous and surface forces:

$$Ca = \frac{\mu_d v}{\gamma} \quad (1.3)$$

here, μ_d is the viscosity of the defending fluid, γ is the surface tension and v is the injection speed calculated at the outer edge of the cell as:

$$v = \frac{\Gamma \phi \pi R_s^2}{2\pi R_c h} = \frac{\Gamma \phi R_s^2}{2R_c h} \quad (1.4)$$

where ϕ is the injection speed of the syringe pump, R_s is the radius of the syringe, R_c is the radius of the pore space, h is the thickness of the cell and $\Gamma=0.5$ is a correction factor accounting for the porosity of the samples.

1.5 Minkowski functionals

I want to quantitatively compare experimental and simulated patterns. In order to make rigorous comparisons, I use the Minkowski functionals to describe my invasion patterns [83]. These can be used to characterize all kinds of complex patterns arising, for example, from dewetting phenomena or fracture [84, 85]. In two-dimensional systems, three functionals are needed to characterize a pattern. These are: (*i*) the ratio of one phase to the total area available, e.g. the liquid saturation, S ; (*ii*) the ratio, α , of this area to its perimeter and (*iii*) the Euler number, E . The last metric is related to the topology of the pattern, and gives the difference between the number of connected regions and the number of holes within them. These three metrics can thus give us information about the filling state of the system at a given time (S) the roughness of the invasion front (α) and the connectivity of the dry phase (E).

In our processed images the saturation, S , is the fraction of the total area covered by the liquid phase (the black pixels) divided by the total area of the porous medium. I note that the boundary layer and the filling channels are excluded from this calculation. In the case of α , I consider only the shape of the leading front. This is defined by the air-liquid interface of the main cluster, which consists of all the wet pores that are connected with the reservoir at the back of the cell. The leading front has a perimeter length P_0 and thus divides the cell between the main, fully wet cluster, and a region of area A_0 which is either dry or contains isolated clusters of fluid. The fraction of the porous medium covered by the main cluster also gives us the main cluster saturation, S_0 . The ratio of the leading area and perimeter, α , can be scaled to be non-dimensional

using the characteristic grid size, a , as:

$$\alpha = \frac{A_0}{aP_0} \quad (1.5)$$

A high α therefore means a small P_0 and corresponds to a compact front. A rough front would show a lower ratio as I show in Fig. 1.4.

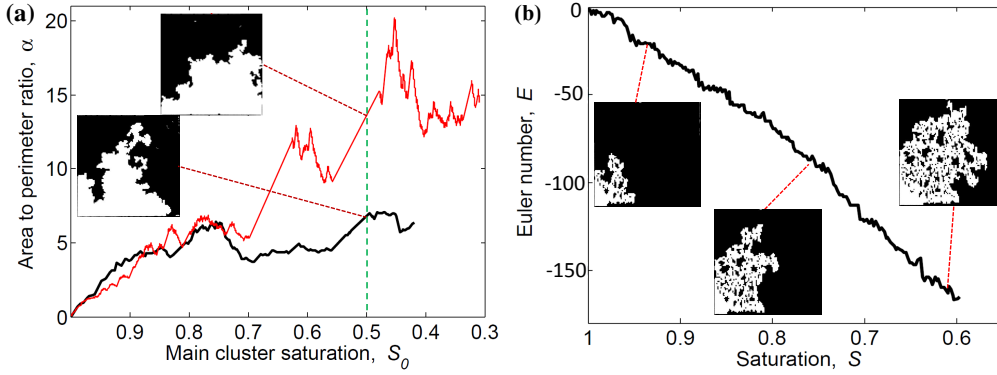


Figure 1.6: Example of how the Minkowski functionals work. (a) The area to perimeter ratio, α , plotted against the main cluster saturation, S_0 , describes the evolution of the drying front in time. For a given invaded area, a smaller α means a higher perimeter and a rougher front, while an increase in the invaded area will show up as an increase in α . Whenever a cluster is cut off from the main cluster, then both α and S_0 will be discontinuous and jump to new values. (b) The Euler number, E , is the number of connected objects (white areas) minus the number of liquid clusters (black areas). Therefore, a low E means that there are many isolated clusters.

Finally, the Euler number is computed by counting the number of connected regions (the dry area, in our case) and subtracting the number of holes (all the isolated clusters). Therefore, the more negative the Euler number is, the more isolated clusters I have.

1 Materials and methods

The metrics presented in this section allow us to characterize the patterns arising in our experiments. In the next chapter I will briefly illustrate the models used to simulate the same experiments.

2 Models

In this chapter I will describe the models I have tested with my microfluidic experiments. These models are the work of our collaborators from the Hebrew University of Jerusalem. I will first describe the model used to simulated drying experiments and then the model used in the displacement experiments.

2.1 Drying model

Simulations of drying cells are performed using a pore-network model inspired by [40, 50] and developed by Oshri Borgman and Ran Holtzman (Hebrew University of Jerusalem, Rehovot, Israel). The goal is to capture the main features arising in experiments using as simple a description of the pore-scale physics as possible, and a minimal set of rules for how pores interact.

The experimental geometry is modeled as a set of discrete pores, which communicate through throats, or constrictions, as sketched in Fig. 2.1. The sizes of both types of objects, pores and throats, are specified by the experimental design. Defining a pore as the space enclosed by four pillars, the pore volume is $V = (a^2 - \sum_{i=1}^4 \pi r_i^2 / 4)h$ where a is the grid spacing, r_i is the radius of one of the surrounding pillars and h is the thickness of the cell. Throats are the minimum distance between two adjacent pillars. If these

2 Models

have radii r_i and r_j , then the throat size is $\delta_{ij} = a - (r_i + r_j)$.

We assume that two time scales play a role in the drying process, namely those of vapor diffusion and pore invasion. As diffusion is much slower than pore-invasion, we are able to separate these two timescales. In other words, we treat invasion events as effectively instantaneous. Between any two sequential invasion events we model the equilibrium vapor concentration in the dried pore space, and use this to solve for the evaporation rate of the volatile phase – here the evaporating oil. Boundary conditions for the diffusion problem are provided by assuming a saturated vapor density at the air-liquid interface, $\rho = \rho_s$, and that the vapor density at the edge of the diffusive boundary layer (i.e. the open atmosphere) is zero, such that $\rho = 0$ there.

Liquid is removed from the sample through evaporation, at a rate approximated by Ficks first law. Between any two adjacent pores i and j there can be a vapor flux:

$$q = -\ell D \nabla \rho = \ell D \frac{\rho_i - \rho_j}{a}, \quad (2.1)$$

Here q is the flux per unit cross-sectional area (i.e. the total mass transfer rate between the two pores is $q\delta h$), δ is the width of the throat between the two pores and $D = 5 \times 10^{-6} \text{ m}^2/\text{s}$ is the diffusion constant of the liquid vapor in air. Furthermore, the difference in vapor concentrations at the centers of the two pores is $\Delta\rho$, and their center-to-center distance is a . The prefactor ℓ allows us to distinguish between diffusion in the porous medium, and the boundary layer. Between any two pores in the chip diffusion is restricted by the throat width, and we set $\ell = \delta/a$. The boundary layer, of width λ , is instead modeled by an array of effective pores with $\ell = 1$. We compute the vapor concentrations and fluxes in the medium by simultaneously solving for the mass balances

2.1 Drying model

(Eq. 2.1) on all pores. In a steady state this is equivalent to solving the continuity equation $\nabla \cdot q = 0$, or the Laplace equation for vapor concentration, $\nabla^2 \rho = 0$, in the continuum approximation.

Initially, our porous medium is fully saturated with fluid. The potential drying rate in this situation can be solved exactly to be:

$$\dot{e}_{pot} = \frac{DP_{sat}m}{\lambda RT \rho_{liq}} \quad (2.2)$$

where $P_{sat} = 2.1 \times 10^3$ Pa is the saturation pressure of our oil, $\rho_{liq} = 1614$ kg/m³ is its liquid density, $m = 0.414$ g/mol is its molar mass, R is the universal gas constant and $T = 298$ K is the lab temperature. The initial drying of the PNM reduces to this situation in the limit of small pores and a thick boundary layer ($\lambda/a \gg 1$).

In order to model pore invasion we approximate the air-liquid menisci of interfacial throats as ellipsoidal caps. These caps are characterized by a dynamic horizontal radius of curvature, limited by the throat size δ , and a fixed, vertical radius of curvature, set by the cell's thickness, h . The pressure-volume relation in such caps is given in [17], and we assume a perfectly wetting fluid phase. As evaporation occurs liquid is removed from the fluid-filled pores, causing their pressure to increase, along with the curvature of the menisci in the interfacial throats. For every throat there is a critical pressure that is set by the Young-Laplace equation:

$$p_c = \gamma \left(\frac{2}{\delta} + \frac{2}{h} \right) \quad (2.3)$$

where $\gamma = 16.2$ mN/m is the air-liquid surface tension. Once the critical pressure is achieved at any pore along the fluid-air interface, then that pore is invaded and its liquid

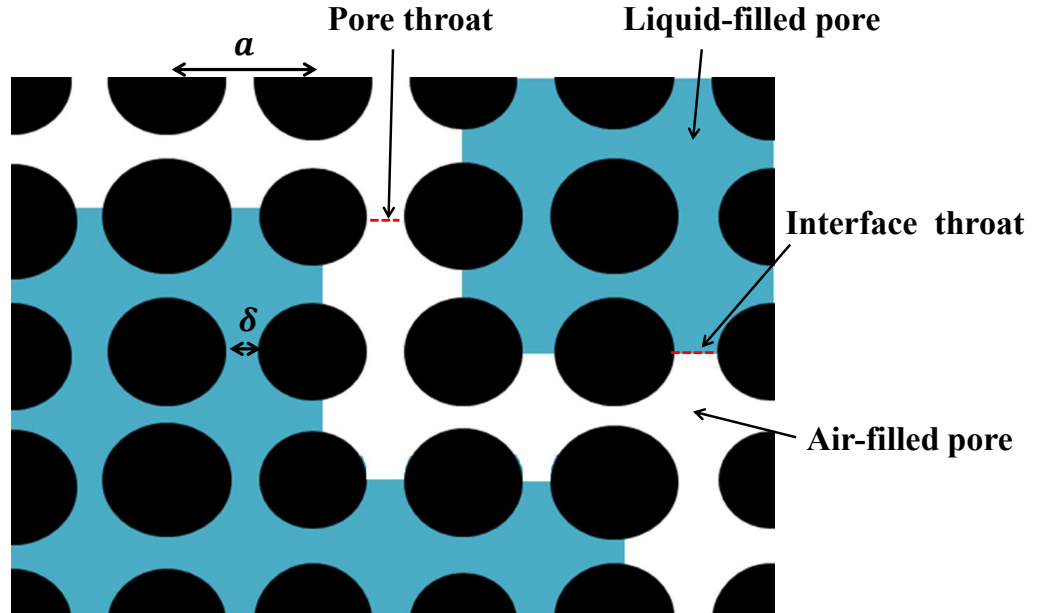


Figure 2.1: Schematic description of the pore-network model, based on the geometry of microfluidic cells. Pillars (in black) of different radii are placed on a grid, with a lattice spacing a between adjacent pillar centers. Pores may be either liquid filled (here, blue) or gas filled (white). Any two adjacent pillars, i and j , are connected by a throat, of size $\delta = a - (r_i + r_j)$. Each connected cluster of pores has capillary pressure p , related to the curvature of menisci in throats along its fluid-air interface.

volume is redistributed among all the saturated pores connected with it. Although this is a simple model, we show in Fig. 3.1 that it can nonetheless faithfully capture many macroscopic details of the experimental drying patterns.

In summary, the algorithm used follows these steps:

1. We calculate vapor densities in the boundary layer and invaded pores to derive evaporation rates from interface pores.
2. We select the next minimum time step needed to reach the next critical interface curvature based on the drying rate.
3. Liquid mass is removed from liquid-filled interface pores.
4. Liquid is redistributed to neighboring pores based on the pressure-volume relationship given in [17], interface curvature in invaded pores is set to zero and we go back to step 1.

2.2 Displacement model

In this section I describe the model that has inspired my immiscible displacement experiments as was developed by Ran Holtzman (Hebrew University of Jerusalem, Rehovot, Israel). Matching experiments and model is a work in progress, therefore there may be some discrepancies between the geometrical assumptions in simulations and experiments. Here I describe the model as it has been used so far [26, 40, 25]

We simulate immiscible fluid-fluid displacement in a disordered porous medium. We construct a two-dimensional heterogeneous medium by placing cylindrical solid particles on a triangular lattice with spacing a . The choice of a triangular lattice allows only up to two menisci to invade an unfilled pore, capturing the essence of cooperative pore filling (as schematized in Fig.2.2) while maintaining simplicity in the algorithm. We select the particles radii, r , from a uniform distribution. Each lattice cell, formed by a particle triplet, defines a pore with volume V connected to three neighboring pores by throats with aperture δ .

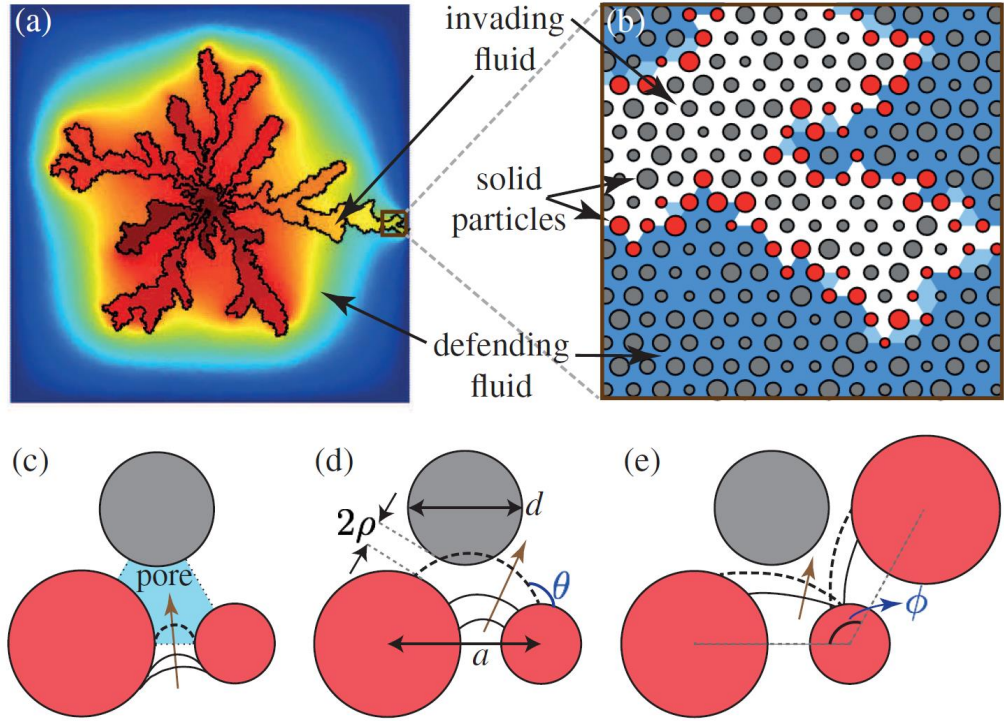


Figure 2.2: Reproduced from [26]. Fluid-fluid displacement in a granular material is modeled (a) by implementing a triangular grid of round particles with random radii chosen within a given uniform distribution (b). Three invasion mechanisms are allowed, Haines jumps (c) where a fluid invades a downstream pore after reaching a critical curvature, touch (d) where a meniscus simply touches the next downstream particle and overlap (e) where two menisci from adjacent throats collide within a pore.

This numerical model provides a mechanistic description of invasion dynamics including both capillary and viscous forces as well as wettability effects. This is made possible by combining two pore-scale modeling approaches. First, a dynamic pore network modeling that resolves pore pressures and pore fluxes from pore topology and geometry (in a way very similar to the model we have used in our drying simulations)[29]. Second, as

2.2 Displacement model

opposed to its drying counterpart, an algorithm that uses the shape of the solid particles in order to compute the meniscus curvature and stability [86]. The combination of these two approaches allows us to simulate a wide range of properties and conditions such as different flow rates, wettability and viscosities.

We model a fluid-fluid interface by a sequence of circular menisci intersecting adjacent pillars at the prescribed contact angle with a curvature $1/R$ supporting a capillary pressure $\Delta p = \gamma/R$. For cells' thicknesses comparable to the throat aperture the meniscus is approximated as hemispherical [26].

We consider three types of menisci instabilities [28]: *Haines jumps*, when the curvature exceeds the threshold set by Laplace's equation; *touch*, when a meniscus intersects the third pillar delimiting the pore while not reaching the critical pressure and *overlap* of adjacent menisci invading a pore at the same time. The two latter mechanisms are possible due to inclusion of wettability effects in the model. The order in which these instabilities are treated has been found to have a minor effect on the results in [28, 29]. In our case, invasion and overlap precede bursts, as the former two happen at pressures lower than the critical pressure set by Laplace's equation.

As a first step, unstable menisci invade adjacent pores. Pore pressures are evaluated from the curvature of the menisci and liquid volume is readjusted via flow throughout the network of pores occupied by the same fluid and through throats with unstable menisci. Stable menisci can be displaced slightly by the readjustments. However, these small displacements are ignored unless these menisci are unstable.

Flow is evaluated through conservation of mass for an incompressible fluid in each pore, $\sum_j q_i = 0$, summing over all connected pores j . The flow rate from neighboring pores is

2 Models

evaluated assuming Stokes' flow, $q_j = C_j \nabla p_j$ where $C \sim \delta^4 / \mu_{eff}$ is the conductance. C depends on the effective viscosity defined as $\mu_{eff} = (\mu_i - \mu_d)\Phi + \mu_d$, where d and i refer to the defending and invading fluid viscosities respectively and $\Phi \in [0, 1]$ gives the filling status of a pore (zero corresponding to an empty pore). The conductance of the porous material therefore depends on δ and Φ .

We assume most of the resistance to flow occurs over a length $\Delta x_j = \delta$. Therefore the pressure gradient $\nabla p = (p_j - p) / \Delta x_j$ is computed from the pressure difference between the two pores. In the case of two pores containing different fluids we use the capillary pressure and front readjustments are included by allowing partial filling of pores which can in turn re-empty when the direction of advancement of menisci is reversed.

In summary this models applies the following algorithm: at each time step we

1. locate the position of the front from the filling status, Φ , and define the flow network;
2. evaluate pore pressure, p , and flow rate, q ;
3. check for meniscus instabilities and update the flow network accordingly;
4. update the filling status, Φ , of each invaded pore with unstable menisci

The time step is chosen so that only a fraction of pore volume is filled, allowing us to capture the disparate time scales of pore filling and bulk flow [55, 56]

We can vary three parameters in this model: disorder, flow rate and wettability. Experimentally though, only disorder and flow rate were actually changed. In [26] and [25] $r \sim 0.25a$ and the cells had a size $L = 100a$. In [25] it is stated that for smaller domains,

2.2 Displacement model

as is the case in our experiments, finite size effects can become dominant and quantitative results would change significantly with the system size.

The models described in this chapter inspired the experiments presented in this thesis. In drying experiments we were able to match sample designs exactly (within the manufacturing sensitivity) whereas matching experiments and simulations of fluid-fluid displacement phenomena is still a work in progress. With this in mind, I will compare experimental and theoretical results in the next chapter.

3 Results

The main goal of this project is to test how well quasi two-dimensional microfluidic cells can describe various complex pore-scale processes and evaluate the effect of pore-scale disorder on such processes. This chapter is split in two parts. The first will deal with drying in porous materials, while the second part will show the results obtained when studying immiscible fluid-fluid displacement.

3.1 Drying

In this section I present two sets of drying experiments. The difference between the sets consists in the way I introduced disorder in my cells. Initially I check how reproducible my experiments are and how they compare with the simulated drying rates. Then I go into more detail on how the medium's heterogeneity influences drying by investigating uniformly distributed random disorder and normally distributed correlated disorder. Finally, I assess some of the problems that arise when comparing experiments and simulations.

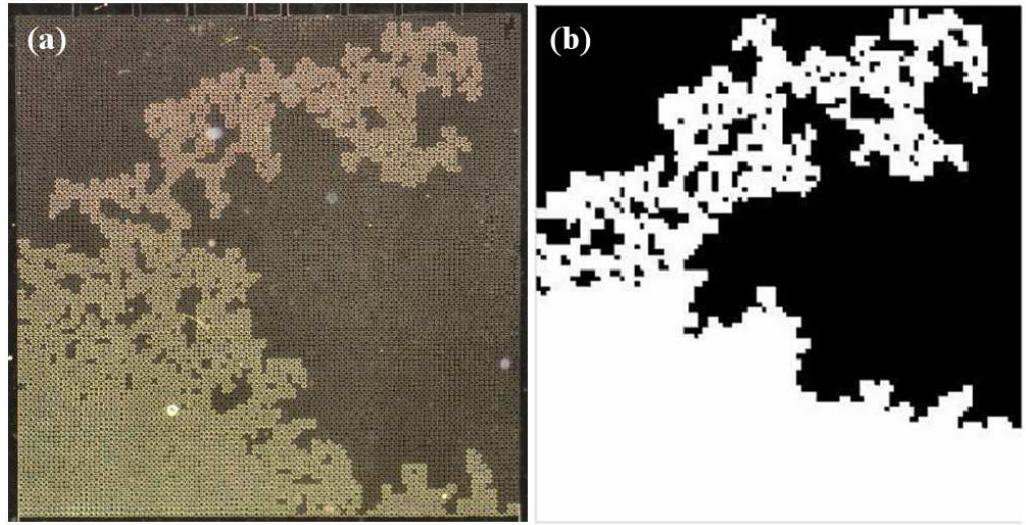


Figure 3.1: Comparison between experimental (a) and simulated (b) patterns at breakthrough. Shown is the level of agreement in the patterns we can achieve when comparing simulations and experiments with matching designs.

3.1.1 Reproducibility control

In this section I compare my results with a simple pore network model. At first I investigate the initial drying rates of filled (fluid-saturated) cells, to check our understanding of the diffusive boundary layer through which evaporation occurs and the initial stage of drying with a constant rate. However, more generally, I also want to reproduce the patterns arising during drying as described by a range of quantitative metrics. In the next section I thus start by comparing absolute drying rates. I then proceed to test how reproducible my idealized experiments actually are and the corresponding sensitivity of our model.

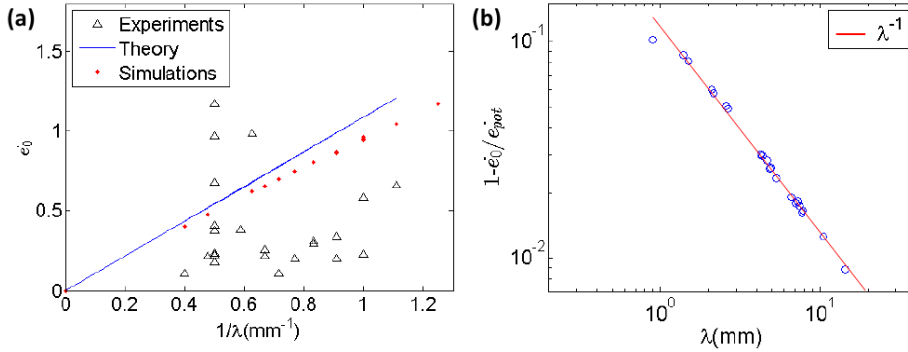


Figure 3.2: The initial, absolute drying rates should scale with the inverse of the boundary layer length, λ . In (a) the blue dots refer to the simple theoretical prediction of Fick's law (Eq.2.1). The red dots show the simulated rates and the black triangles the experimental initial drying rates. In (b) we show how the theoretical and simulated rates approach each other asymptotically, as reported in [17].

Drying rates

I fill my NOA cells with Novec 7500 Engineered Fluid (3M), a fluorinated, volatile oil with almost-perfect wettability (contact angle measurements gave an angle between 0° and 3°). A saturated cell is sealed at the inlet in order for evaporation to occur only from the open boundary. Once the cell is filled and its inlet is sealed, I let it dry horizontally while the camera takes a picture every minute. An experiment begins with the onset of air invasion into the drying porous medium. In all of my experiments I observe an initial phase (of at least 40 minutes) where the drying rate, $\dot{\epsilon}$, is constant within experimental uncertainty. The duration of this constant rate period depends mainly on the size of the boundary layer, as for the early drying the pore geometry of the cell is expected to have little to no effect on the drying dynamics[17].

3 Results

The experimental evaporation rates have two main sources of error: variations in the height of the boundary layers that may be introduced while sealing the samples (e.g. bending of the substrate) and noise due to the discretization and measurement of the time-lapse images. Otherwise, experiments were carried out in well-controlled conditions, with the temperature being fixed to within ± 1 °C. Considering the measurement error first, I found that during the initial drying period the measured drying rate would naturally fluctuate with an average standard deviation of $0.12 \mu\text{m s}^{-1}$ around the mean rate, in any particular experiment. I take this as my absolute measurement uncertainty. However, as shown in Fig. 3.2, it is clear that the systematic variation in conditions between experiments is more important. In fact, the data at $\lambda^{-1} = 0.5 \text{ mm}^{-1}$ show how the initial drying rates can vary greatly between experiments even while keeping the boundary layer constant.

In Fig. 3.2 I show how the experimental and simulated initial drying rates, \dot{e}_0 , depend on the inverse of the boundary layer's length, λ^{-1} . As well, we show the potential drying rate given by Eq.2.2. In the simulations the drying rate is extracted by solving for the vapor density in the boundary layer and then computing the vapor mass flux in the pores along the air-liquid interface. For evaporation off of a pool of fluid the drying rate should scale inversely with the boundary layer's length, as described in Eq.2.2. For evaporation over a wet porous body, \dot{e}_0 is expected to be slightly lower, by an amount that depends on the ratio of the pore size to the boundary layer width and the relative coverage of pores at the surface [17]. However the ratio of drying rates from a free fluid and a porous surface should asymptotically approach one as the boundary layer increases: such behavior is demonstrated in Fig. 3.2b .

When compared to experiments, the simulations capture the right order of magnitude of e_0 , although experiments typically show a lower initial drying rate (about half that expected). This discrepancy between model and experiment can be reduced if we consider an additional effective boundary layer of about 3 – 8 mm. The difference could thus be accounted for by the existence of a small additional effective boundary layer in the stagnant air outside the microfluidic chip, with additional (and unmodeled) gradients in the vapor concentration there.

As we will show in the next sections, however, uncertainties in the effective boundary layer width affect the initial drying rates alone and will not significantly change the patterns formed during drying. Therefore, in order to simplify further analysis and comparisons, we will use these initial drying rates to scale our observations as described in the *scaling* section.

Repeatability

Here, I examine the reproducibility of the drying patterns experimentally. A source of uncertainty in the experiments is the manufacturing of the cells. Therefore, we want to know: how well does the pillar size distribution in a chip match its design? Then, we estimate how much this error influences a drying pattern, in order to answer the question: will the metrics stay the same for different copies of the same master design? To answer the first question, I compared digital microscope pictures of my samples with the designs of their masks, as sketched in Fig. 1.1. Measuring the size of 200 pillars gave an average radius of $49.72 \pm 0.18 \mu\text{m}$, compared to a designed size of $50 \mu\text{m}$. Thus, we have a negligible systematic error in manufacturing of at most $0.28 \pm 0.18 \mu\text{m}$. However, when measuring 50 single pillars and comparing them to their design, I have found their radii

3 Results

to be, on average, $1.63 \pm 0.20 \mu\text{m}$ different from the original design. This corresponds to a 3.2% random manufacturing error in feature size. During manufacture I also measured variations in the thickness of the pore space by means of a white light interferometer. Within each sample, as measured at the four corners, I tolerated variations in thickness of no more than $3 \mu\text{m}$. For this paper all samples were, on average, $38 \mu\text{m}$ thick.

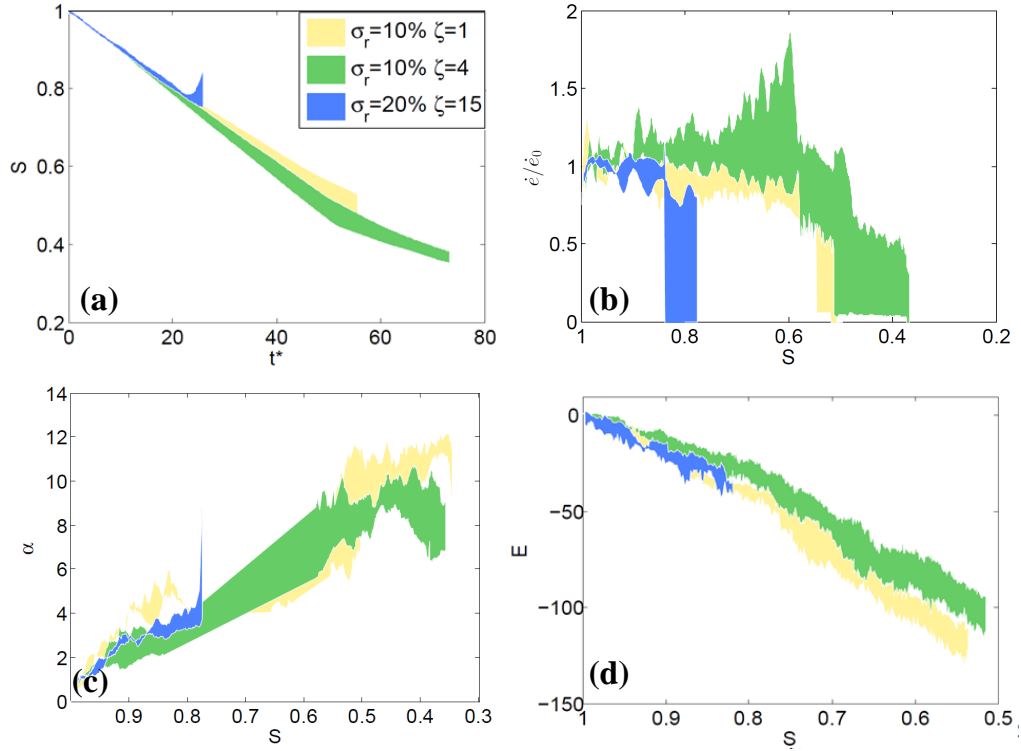


Figure 3.3: Metrics showing the experimental clouds of observations (mean behavior within one standard deviation). We show three clouds, each produced from the same master repeated three times. Shown are: Saturation vs. t' (a); Drying rate vs. Saturation (b); α vs. Saturation (c); Euler number vs. Saturation (d)

The next question was: how reproducible are the drying patterns? I have repeated

experiments on three designs in order to establish the expected size of the experimental cloud of results. I did this by using, for each design, three different chips cast from the same master. I measured the Minkowski metrics during drying in each case and estimated a reproducibility cloud for our experiments. The boundaries of these clouds are established by averaging the results of each of the three samples and calculating their standard deviation. An example of the experimental clouds thus established can be seen in Fig. 3.3, where the colored areas show the range of my tests. We can see how the same design tends to follow the same path despite minor experimental variations.

To determine how well the exact drying patterns can be reproduced I also compared experiments pore-by-pore using the matrices shown in Fig. 1.3.2d.2. In order to do this I first used the pore invasion matrix, T_{ij} , to find which pores had been invaded at any time t_0 as

$$A_{ij} = \begin{cases} 1 & T_{ij} \leq t_0 \\ 0 & T_{ij} > t_0 \end{cases}$$

I then confined my attention to the invasion pattern of the main cluster by removing from A_{ij} all isolated clusters, namely, isolated patches of ones. At the same main cluster saturation S_0 . I could then compare two invasion patterns A and A' by computing their overlap, or match

$$\Delta = \frac{A_{ij} \cdot A'_{ij}}{N}$$

where $N = \sum_{i,j} A_{ij}$. In other words, I find the fraction of invaded or isolated pores, Δ , that match each other in both patterns, at the same main cluster saturation.

The evolution of Δ is shown in Fig. 3.1.1 for each of the three replicated experiments. Figure 3.1.1(a,b) shows how the invasion patterns in replicates can be reproduced with a match of up to $\Delta \simeq 90\%$, and typical values of about 80%. In contrast, Fig. 3.1.1 (c)

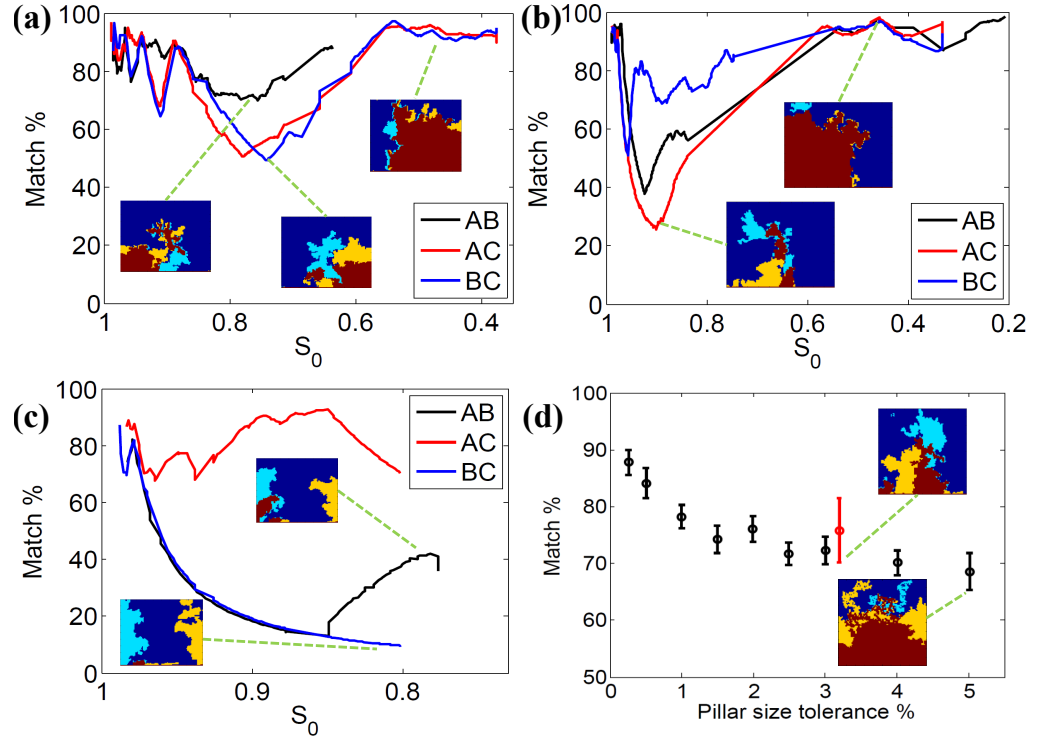


Figure 3.4: Pore-by-pore comparison of the leading patterns during drying. I repeated three experiments for each of three separate designs. In panels (a) – (c) I show how well the drying patterns match each other between pairs of replicates. Insets show the differences in invasion patterns. The colors highlight areas that are unsaturated in both samples (red), in one sample only (yellow or light blue) or part of the main cluster in both samples (dark blue). In (d) I also show how increasing the manufacturing error in our designs decreases the achievable match in the leading patterns of numerical simulations when $S_0 = 0.5$. The red point compares this with the average agreement between our experiments and their corresponding simulations when $S_0 = 0.5$ (see Fig. 3.7).

shows a case where the similarity of the patterns is lower than $\Delta = 10\%$ at breakthrough. However, the insets explain why: drying in this particular sample reached an early binary choice, based on the near-surface pore sizes and evolved the drying front either on the left (replicates A, C) or the right side (replicate B) of the cell, hence the lower Δ .

In order to predict the agreement that could be expected between experiments and numerical modeling, we also tested how a random manufacturing error may affect the invasion patterns during drying. For this, my Oshri Borgman ran a series of numerical simulations with the same initial geometries (radius distributions with relative width $\sigma_r = 0.2$), but additional random perturbations in the pillar sizes. Figure 3.1.1(d) shows the match we were able to achieve between different numerical simulations when introducing such a random error. There, we see how increasing the manufacturing error gradually reduces the possible match between patterns, going down to 70% when as little as 5% error was introduced.

Sensitivity analysis

Here, together with our colleagues from the Hebrew University of Jerusalem, we use simulations to evaluate the sensitivity of our system to several control parameters. Some parameters, like throat aperture and boundary layer length, are easier to control experimentally than others, like temperature, air pressure and relative humidity. In order to check that our scaling correctly accounts for uncertainties in the room conditions while leaving in all geometrical effects, we chose one particular experimental geometry to model, then individually varied (i) the vapor diffusivity D , (ii) the vapour saturation pressure P_{sat} , (iii) the mean throat size δ and (iv) the boundary layer width λ and observed how the saturation-time curve changed. The results of this sensitivity analysis

3 Results

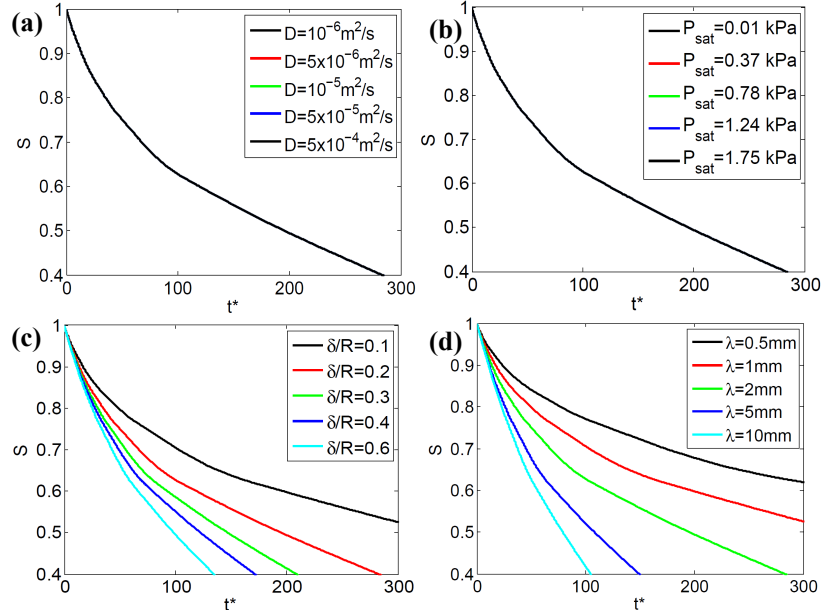


Figure 3.5: I show how the saturation-time curves vary when using a time t^* scaled by the initial evaporation rate, as parameters change in our model. The parameters are the diffusion coefficient, D (a), the vapor saturation pressure P_{sat} (b), the throat aperture-to-pillar radius ratio, δ/R_{mean} (c) and the boundary layer's width, λ (d). When varying D and P_{sat} the drying curves collapse. However, changing the mean throat size or the boundary layer's width has an effect on how quickly drying slows down over time.

are shown in Fig.3.4

From Fig. 3.4(a-b) it is clear that D and P_{sat} have no additional effect on drying beyond the scaling of Eq. 2.2 and that this effect is accounted for entirely by our choice of dimensionless time. However, changing the throat aperture or the boundary layer's thickness does result in a different behavior.

Changing the throat aperture changes vapor transport properties in the model, as shown in Eq.2.1. In Fig. 3.4(c) I show how decreasing δ/R_{mean} and, consequently,

offering more resistance to the vapor transport within the medium (as compared to the surface boundary layer), causes the drying rate to slow down more, as the drying front recedes into the porous medium. This effect is not surprising, as it proves how the throat sizes regulate transport within the porous medium.

Changing λ also causes the drying rates to slow down at different paces. Specifically, a thicker diffusive boundary layer effectively separates the porous medium from the atmosphere by a long diffusion path. When this remains large, as compared to the diffusive path through the pore space, evaporation will stay roughly constant. Conversely, for a short boundary layer, the drying rate will vary more as the drying front recedes from the surface.

3.1.2 Uniformly distributed random disorder

Having characterized the variations expected in both experiments and simulations, I will now compare the two cases to each other directly via their drying rates and Minkowski metrics. For this test I also changed the amount of disorder in my cells to test the effects of local heterogeneity on drying. As discussed in the methods section, I generated distributions of pillars where I allowed the radii to change within a 3, 5, 10 and 20 % window. Two different randomizations of the pillar radii were made for each level of disorder, with different random seeds. The same exact geometries were then reproduced in our simulations. In Fig. 3.5(a) we first compare drying curves as a function of the dimensionless time t^* and then the relative evaporation rates as a function of the liquid saturation, S . In each plot we compare experiments (solid lines) and simulations (dotted lines). Lines of the same color within the same plot refer to the same sample geometry.

There was no clear effect of disorder on either the saturation-time curves or on how the

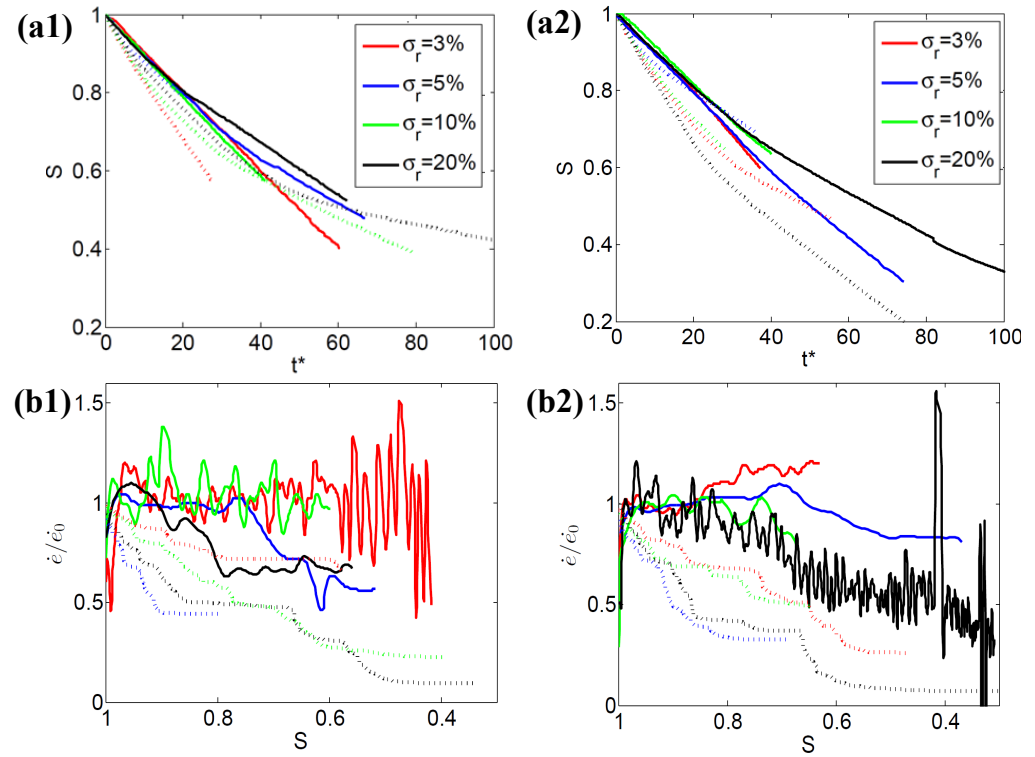


Figure 3.6: Saturation and drying rates of samples with varying degrees of disorder. The left column (1) shows one set of experiments, while the right column (2) shows a re-randomization of the same experiments. Solid lines refer to experimental results, whereas dotted lines (of the same color) show corresponding numerical simulations, using the same pillar sizes.

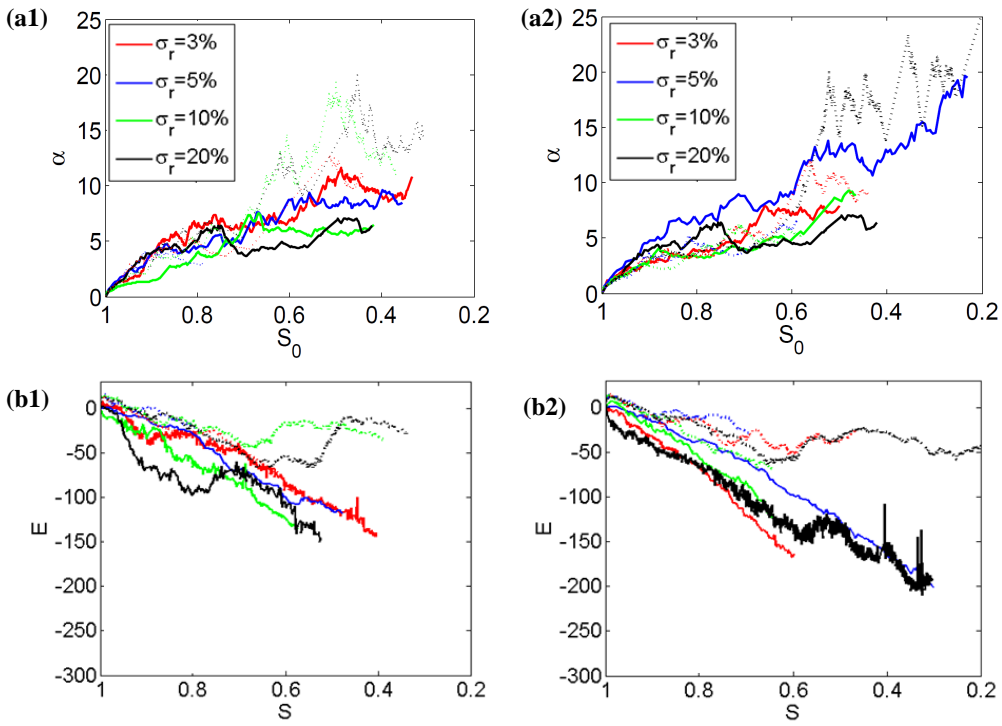


Figure 3.7: Minkowski functionals for two different re-randomizations (columns (1) and (2)) and levels of disorder. Panels (a) show the area-to-perimeter ratio, α , vs. main cluster saturation S_0 and (b) show the Euler number, E , vs. saturation, S . Line colors and types are as in Fig. 3.5.

3 Results

evaporation rates of the samples evolve. However, we observed that experiments would always start by keeping a constant rate period and that, in some instances, the beginning of the falling rate period can be seen before breakthrough. In contrast, the simulated evaporation rates always drop immediately. They usually then stabilize around a value of 0.4-0.8, and later drop again. In order to understand the origin of this discrepancy we further compare drying patterns by using the Minkowski functionals.

We show how the functionals evolve during drying in Fig. 3.6. The roughness, α , of the leading front as a function of the main cluster saturation, S_0 , is reproduced well in the simulations, increasing in a very similar way to that observed experimentally. However, the dynamics of the Euler number, E , are not reproduced as well. In the experiments, the receding drying front leaves behind large numbers of clusters that evaporate very slowly. In contrast, fewer isolated clusters form in the simulations and these clusters disappear faster than in the experiments. The difference in the behavior of isolated clusters could explain the discrepancy observed in the experimental and simulated drying rates. For example, the persistence of the isolated clusters in the experiments effectively maintains higher drying rates by increasing the vapor concentration and enhancing transport within near-surface pores. I will test this idea further in a later section.

Since the patterns seem to affect the drying rates, I have quantified their discrepancies more precisely by making a pore-by-pore comparison between experiments and simulations as I did when comparing single experiments in Fig. 3.1.1. This result is summarized in Fig. 3.7. There we see how most experiments stay within, or at least close to, the limit of $\Delta = 70\%$. This is a good result when compared to the $\Delta = 90\%$ threshold at breakthrough we established in the *Reproducibility* section. In figure 3.1.1(d) I actually show how a manufacturing error of 3% (which I measure in my samples) brings the best

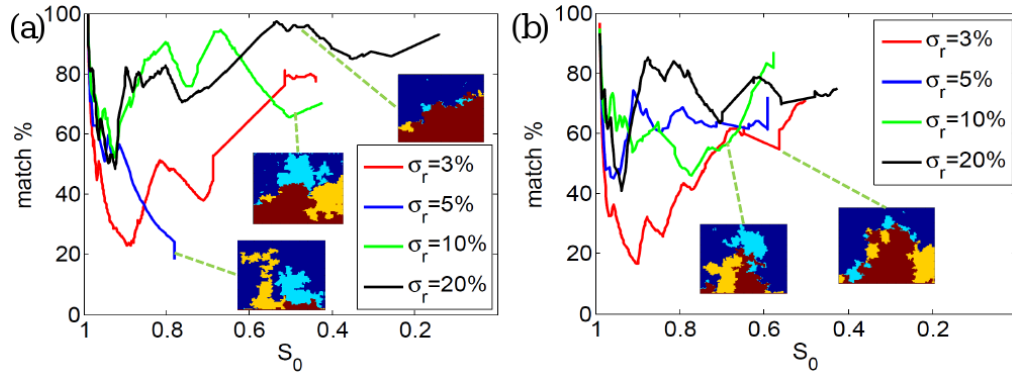


Figure 3.8: pore-by-pore comparison of leading patterns. The plots show the difference in number of open pores, expressed as a percentage, versus S_0 . Shown are two different randomizations (a),(b).

possible agreement in the 70-80% range. Therefore a 70% match is as close to a perfect agreement as it is possible to achieve, given my experimental tolerance. There is one exception where Δ very quickly decreases reaching a value lower than 30% and does not increase again before the front reaches breakthrough. Although not as markedly as in Fig. 3.1.1(c), we can see from the insets the case where this happens is similar to that, where the front evolves as a consequence of an early binary choice over which side of the cell to invade. This is also a demonstration of the high sensitivity of the invasion pattern on the exact details of the sample geometry. Making even a single pore smaller can, in fact, force the front to evolve very differently from the way predicted by the simulations.

3.1.3 Normally distributed correlated disorder

In this section I will show the results we obtained by introducing correlated heterogeneity in our cells. These particular experiments were carried out by Wieland Lühder in his Bachelor's dissertation [82]. We have produced cells with different amounts of disorder

3 Results

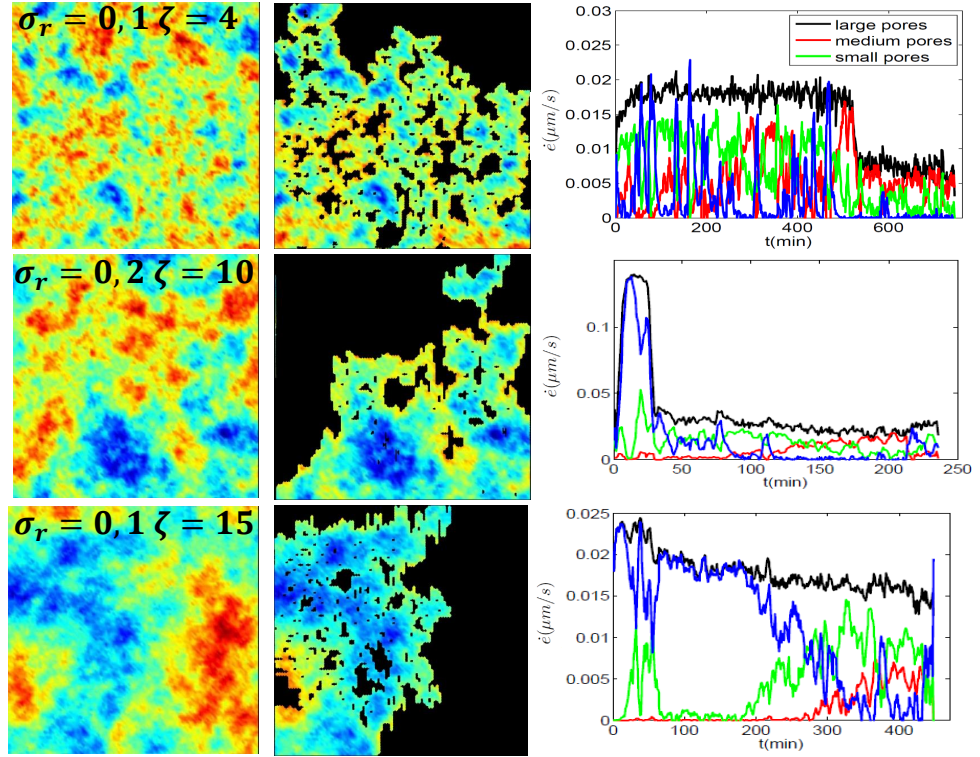


Figure 3.9: I show color maps of three different samples (left column), their invasion patterns masked with such color maps (middle column) and their drying rates (right column) divided into total drying rate (black line) and drying rates of large (blue), intermediate (green) and small (red) pores.

and correlation lengths. There is a total of eight experiments grouped by the amount of disorder, 10 and 20%, and with correlation lengths of $\zeta=1, 4, 10$ and 15 pillars.

The most immediate result is that the front is somehow guided by the porous medium geometry. An example of this is shown in figure 3.8. There we show a color map of the pore size distribution, where blue corresponds to large pores, red to small pores and green to intermediate size. When masking the color map with invasion patterns it is

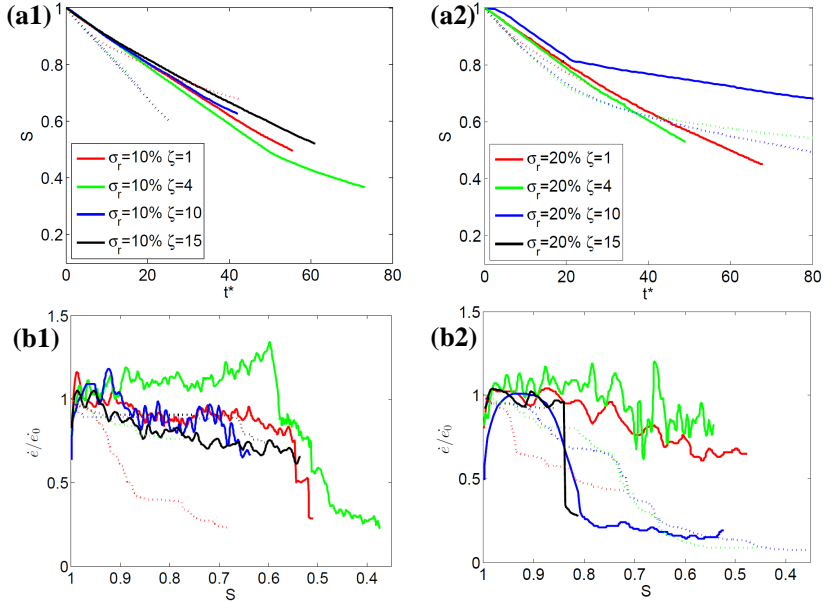


Figure 3.10: We show a comparison of saturation and drying rates of experiments and simulation with correlated disorder. The plots refer to a disorder $\sigma_r=10\%$ (1) and $\sigma_r=20\%$ (2). Solid lines refer to experiments whereas dotted lines of the same color show simulated results of corresponding cell geometries.

evident how the dry area tends to preferentially invade larger pores. In order to have a more rigorous test for this, I show the total absolute drying rates (black line) and the absolute drying rate of large, intermediate and small pores. In figure 3.8 one can see how the large pores contribute to most of the total drying rate while intermediate- and small-sized pores only start to be invaded at later stages. Another interesting feature is the alternate behavior of the size-dependent drying rate. One can see how, when the drying rate of large pores drops –meaning the drying front has run out of *large* options– there is a burst in the drying rate of small pores and this lasts as long as a new patch of large pores is available. I have checked how simulations capture the drying rates and the patterns forming in these correlated cells. The results are shown in figure 3.9 and 3.10.

3 Results

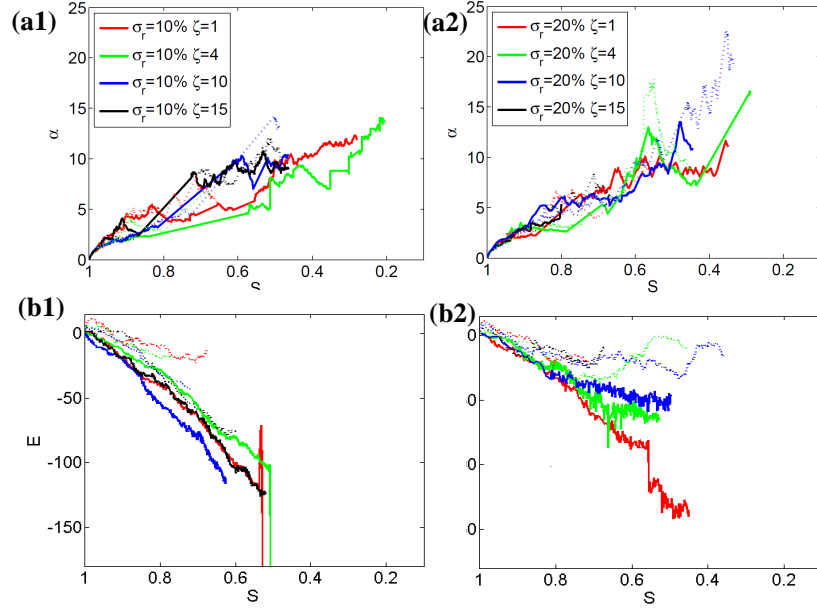


Figure 3.11: We show a comparison of the Minkowski functionals of experiments and simulations of samples with correlated disorder. The plots refer to a disorder $\sigma_r=10\%$ (1) and $\sigma_r=20\%$ (2). Solid lines refer to experiments whereas dotted lines of the same color show simulated results of corresponding cell geometries.

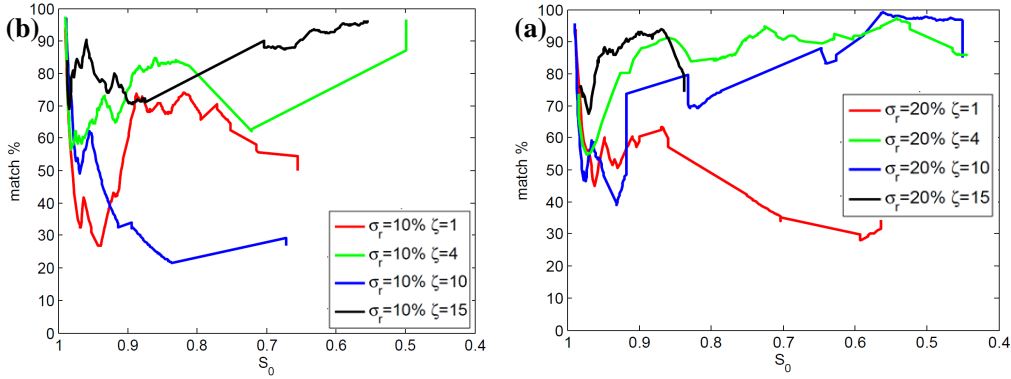


Figure 3.12: Pore-by-pore comparison of experimental and simulated patterns with correlated normal heterogeneity

The drying rates do not seem to be reproduced better in cells with correlated disorder than they were in their random counterpart. If we look at the Minkowski measures we see an analogous result to that of random disorder: we do a good job when trying to capture the leading pattern while the number of isolated clusters is still higher in the experiments than it is in the simulations. As we did for uncorrelated samples, we have compared the patterns pore-by-pore. We show the results of this comparison in Fig. ?? as was the case in samples with uncorrelated heterogeneity, we measure a match of leading patterns of 60 % or better in most cases, which, compared to the threshold of 60–70% established in Fig. 3.1.1d, is an excellent result.

We have seen how for both random and correlated disorder we seem to have some obvious discrepancies between experiments and simulations. Specifically in the formation and persistence of isolated liquid clusters and in the drying rates. These quantities however are related and the isolated clusters can explain the discrepancies in the drying rates. Leading patterns are however captured excellently in light of the achievable manufacturing precision. In the next sections we investigate possible reasons for the

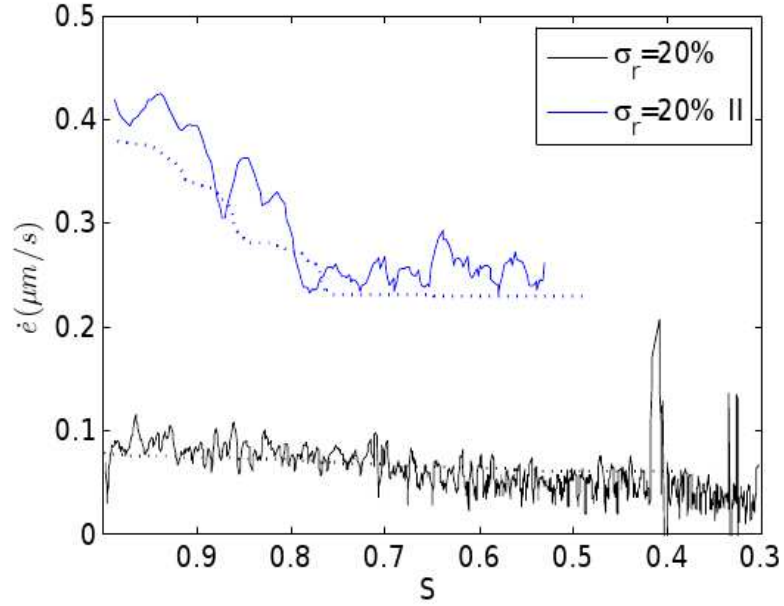


Figure 3.13: Absolute evaporation rates calculated by modelling Laplace's equation for the experimentally observed sequence of drying patterns, for two different trials. Experimental rates are shown as solid lines, while simulated rates are shown as dashed lines.

discrepancies we observe in our results.

3.1.4 Diffusion versus Invasion

The different behavior of drying rates in experiments and simulations can be explained by considering the different way in which isolated clusters form and behave. In the model, these isolated clusters of liquid evaporate very quickly, whereas they are less active in experiments, often persisting until breakthrough. If we take the experimentally evolved patterns, at various times, we can use our numerical model to predict what the resulting evaporation rate should be for those exact patterns. By doing this for each image in the

sequence of a drying experiment, we can test whether the difference between the observed and predicted creation and loss of clusters can explain why the simulated evaporation rates behave differently from the experiments. In the process, we can also implicitly test whether the simulation accurately models diffusion in the pore space of the experiment. I show the results obtained by Oshri Borgman with this procedure in Fig. 3.11, for two typical experiments. This figure shows experimental (solid lines) and simulated (dashed lines) drying rates, where the latter are extracted by taking the experimental pattern sequence recorded in T_{ij} and using it to estimate the drying rate with our model, based on the resulting estimation of vapor concentration gradients. This process clearly improves our estimate, getting experimental and simulated drying rates to agree. The improvement suggests that vapor diffusion is actually well modeled in our simulations, allowing us rule out one possible source of error and focus on invasion mechanisms and the formation of isolated clusters as sources of the observed discrepancy.

3.1.5 Wettability

A potential cause for the more limited appearance and the lack of persistence of isolated liquid clusters in simulations are wettability effects that are not considered in the model. To examine this, we repeated some experiments with a less wetting fluid, water, which has a contact angle of about 70° on NOA [80] (as opposed to the $\simeq 3^\circ$ contact angle of 3M Novec 7500). A highly wetting fluid, like our oil, easily breaks into clusters, especially in the corners between pillars and the walls of our cells, forming rings of fluid around the bases of the pillars. These rings may not influence fluid transport directly, but they could contribute by increasing vapor concentration in pores, thus affecting drying behavior. When the wettability of the fluid decreases (e.g when using a different liquid) the formation of these rings and isolated clusters decreases as well, as a consequence of

3 Results

the higher surface tension of the liquid.

Results are shown in Fig. 3.12, which shows the metrics for one particular experiment run three times with oil (blue cloud) and once with water (black line). It can be seen that the fluid saturations, the area-to-perimeter ratios of the leading fronts, and the drying rates behave virtually the same way in both cases. The only observed difference is in the Euler number. Not only is the final amount of clusters lower when using water, but the number of clusters that are formed is always lower at the same saturation. This shows a higher liquid surface tension alone can limit cluster formation, while not strongly influencing the relative drying rate.

3.1.6 Salt

A further reason for the formation of isolated clusters could be the presence of a non-volatile, dissolved component (e.g. salt) in the oil we have used in our experiments. Such salt would concentrate at the liquid-vapor interface, changing vapor pressure and hindering evaporation. To test this possibility we have tried dissolving several chemicals in Novec 7500. However, the ones that did dissolve had a higher vapor pressure and could not serve the purpose of studying the behavior of the experiments in the presence of a nonvolatile phase. Most chemicals do not actually dissolve in Novec 7500 as it is engineered to be as inert as possible. Because of the difficulties in finding an appropriate chemical, we decided to try and experiment with water saturated with CCaO_3 .

In Fig. 3.13 I show the patterns arising when experiments are carried out with Novec 7500, water and water saturated with salt. When adding salt, the drying front invades an area that was otherwise unexplored in the experiments done with pure liquids (three with oil, one with water).

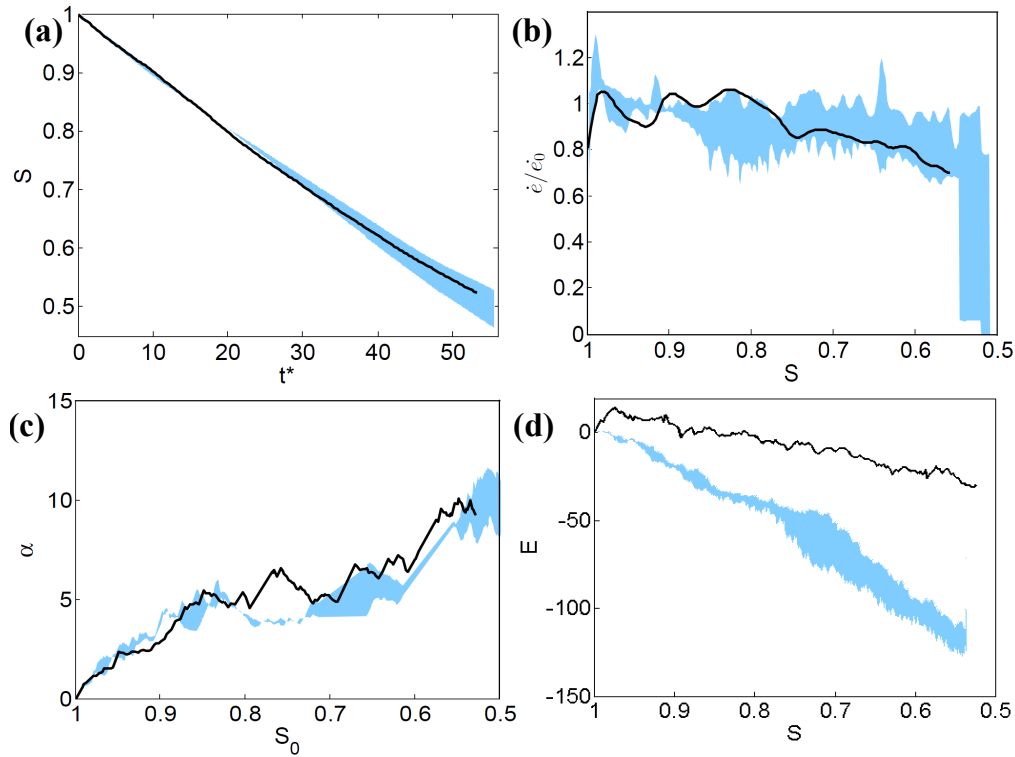


Figure 3.14: Metrics showing the experimental clouds of observations (the blue area gives the mean behavior within one standard deviation). The black line corresponds to an experiment in the same design, but with water, instead of oil, as the volatile phase. Shown are: Saturation vs. t' (a); Drying rate vs. Saturation (b); α vs. Saturation (c); Euler number vs. Saturation (d)

While surprising at first, this behavior is easily explained: salt is indeed concentrated, via flow, at the larger pores because evaporation is more likely to occur at these locations. There, as the liquid evaporates, a precipitate is formed, clogging the pores and excluding them from the drying process, therefore leaving the pores that would have otherwise remained wet as the only possible drying zone. However, the plot in Fig. 3.13 shows how introducing a nonvolatile phase in the liquid did not produce a very different result

3 Results

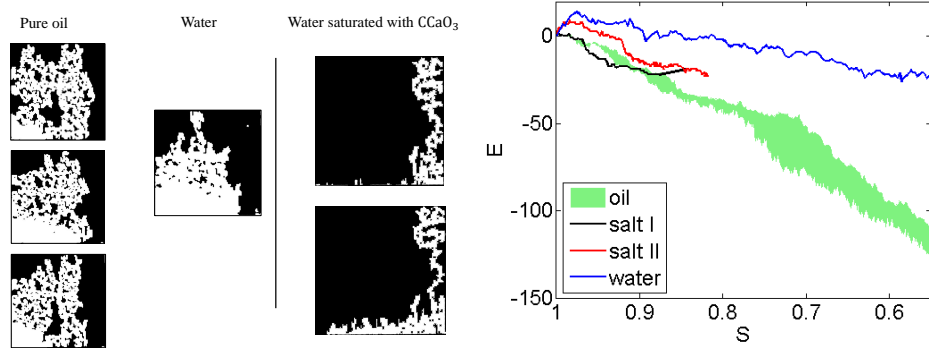


Figure 3.15: Drying patterns with oil, water and water saturated with CCaO_3 . When adding salt the pattern is the inverse of that of pure liquids due to salt precipitating at the largest pores, where evaporation preferentially occurs. The Euler number in the presence of salt is however comparable to that found when experimenting with pure water or oil.

in terms of clustering. In fact, two experiments where salty water was used gave a comparable number of clusters to that found in their pure counterpart. This result allows me to exclude the presence of nonvolatile contaminants in the oil I have used for my experiments.

3.2 Immiscible fluid-fluid displacement

In this section I will illustrate a different kind of experiments: immiscible fluid-fluid displacement.

The microfluidic design is similar to that used in drying experiments, consisting of a porous medium made of circular pillars. The grid is now triangular. I have produced four designs three where the pore-size distribution is stretched between samples with different amounts of heterogeneity in order to minimize the effects of geometrical sample

3.2 Immiscible fluid-fluid displacement

details of a specific random seed and one was a different realization (seed) of a specific amount of heterogeneity. Therefore we have samples with heterogeneity 3, 20 and 37% of the mean radius with the same relative pore sizes and one reseeded sample with 20% heterogeneity.

The experiments are summarized in the phase plot in figure 3.14.

When compared to previous, similar experiments in Fig.3.14c (reproduced from [25]) we observe similar results for similar Ca . We point out that the experimental procedure in [25] was slightly different in the way air was displacing water. There, the invading fluid was freely expanding into the pore medium by sucking the defending fluid out from the samples. This procedure makes air compressibility negligible. Despite this difference, my experiments look very similar to the previous ones, even though the length-scales involved are very different (in [25] the grid spacing was $a = 1$ mm, in my experiments $a = 60$ μm) and the manufacturing precision was considerably higher in my case (Fig. 3.14d).

The model in [25] predicts patterns that only form in experiments at higher capillary numbers than those predicted in simulations. With my setup I was not able to reach Capillary numbers greater than 10^{-3} . However I can already notice how my results start diverging from the simulations. This is most likely due to the lack of compressibility of the invading fluid in the model.

It is of course possible that my experiments could have leaks that may have escaped my control and caused the observed discrepancy. I have investigated this possibility by performing an experiment with the cell and one with the needle of the syringe under water. The absence of bubbles in this situation allows me to exclude the possibility of leaks and conclude compressibility of the invading fluid plays a very important role in

3 Results

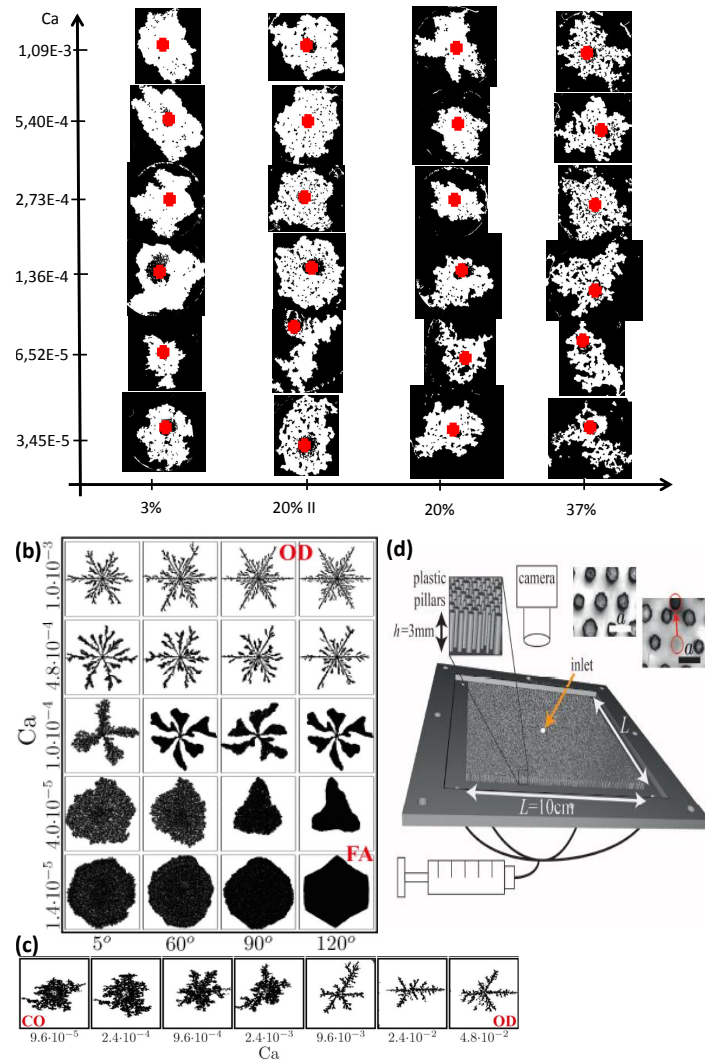


Figure 3.16: Breakthrough patterns of fluid-fluid displacement experiments and model. In (a) I show my experimental results. The red dot marks the injection site on the cell. In (b) I show the results of simulations (reproduced from [25]) and in (c) (reproduced from the same source) I show experiments done at a pore-size disorder of 20%. (d) shows their experimental design and the manufacturing problems they have faced even though they were working at a millimeter scale (grid spacing, a , was 1 mm)

3.2 Immiscible fluid-fluid displacement

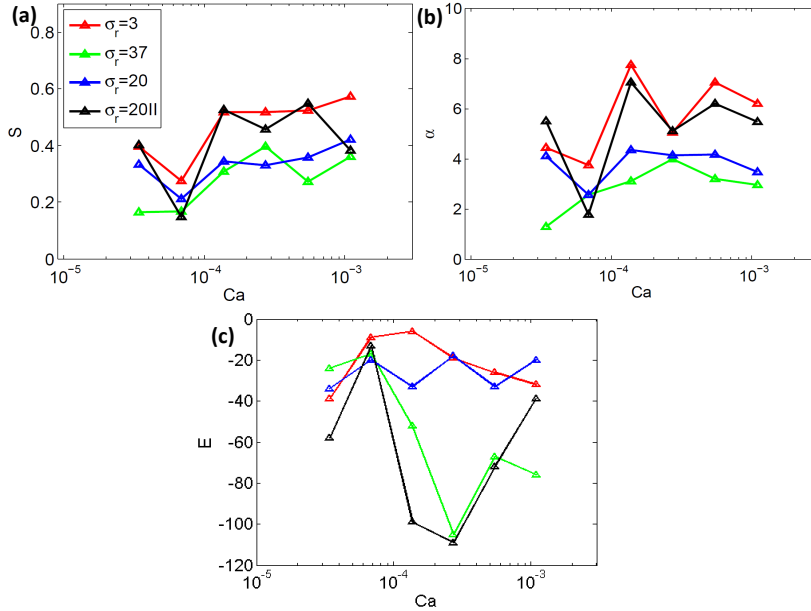


Figure 3.17: Minkowski measures of breakthrough patterns plotted for different capillary numbers. I show (a) Saturation, S ; (b) Area-to-perimeter ratio, α , and (c) the Euler number, E .

immiscible displacement.

I want to investigate the effects of pore size disorder on the patterns formed by the displacement of the defending fluid. For a rigorous comparison of the patterns I rely on the Minkowski measures, which I show in Fig. 3.2 plotted against the capillary number. Due to time constraints, a rigorous comparison to the model in the style of what we have done for drying experiments was not yet possible. However, in agreement with the thesis tested in [25], we can see how increasing disorder seems to produce a rougher invasion front based on the lower saturation and α measured at higher amounts of pore-scale disorder. The Euler number gives a weaker trend, although it seems like a higher disorder may promote the formation of isolated clusters of the defending fluid. However,

3 Results

more experiments and rigorous comparisons with the model are needed to state something conclusive on the matter.

In the next chapter I will discuss the results I have reported so far and offer possible explanations for the discrepancies I have found when comparing to simulations.

4 Discussion

In this chapter I will discuss the results shown so far. I will discuss the successes and the failures in comparing with the model and suggest improvements that could be made to get a better understanding of the problems I am investigating.

4.1 Drying experiments

The goal of these experiments is to provide a novel experimental method to study drying in porous materials. I have used microfluidic cells to make a two-dimensional granular medium with grains of size comparable to that of real soils improving on both the control of the sample geometry of previous works [67, 13], the pore sizes [45, 66] the throat sizes [64, 54, 65] and the number of objects in the porous medium [69]. The improvement was made possible by using microfabrication techniques common in microfluidics [74] that allow precise control over the positioning of micron-scale objects. I have imposed a fixed size distribution heterogeneity on the grains and pores to investigate the effects of disorder on the drying behavior in porous media. In drying experiments, the microfluidic cells were filled with a volatile oil and allowed to dry. Experimental results were compared to pore-network model simulations, a class of models chosen thanks to its ability to combine computational efficiency and description of complex effects [51, 50].

4.1.1 Absolute initial drying rates

The pore network model we have used to reproduce our experiments has some problems capturing the exact drying rates. This result is summarized in figure 3.2. The order of magnitude of initial drying rates, when the porous nature of the system is not as important in the evaporation process [17], is captured well. I attribute the variability of experimental initial drying rates to distortions of the boundary layer's thickness that occur during the manufacturing process, whereas the discrepancy between experimental and simulated initial drying rates can be reduced by considering a small, additional boundary layer extending outside the manufactured cell. I have removed this discrepancy by including it in my scaling of drying rates. Since experimental drying rates are constant in the early stages, I have scaled them with their initial value to extract a non-dimensional quantity to compare to simulations.

4.1.2 Sample reproducibility

Being able to exactly reproduce a sample over and over is important to compare well with simulations. On average I do a fairly good job reproducing average pillar radii within a half micron. Unfortunately, when comparing single pillars to their design I found an average error of $1.63 \pm 0.20 \mu m$ on their radii. That is a huge error when comparing to the more homogeneous samples with a set heterogeneity of 3% (corresponding to $1.5 \mu m$) and it becomes less relevant as the disorder increases. An example of this can be seen in figure 3.7 and ???. There we see how samples with a higher disorder generally match the simulations better throughout the experiment. Furthermore, I show in figure 3.1.1d how even a small ($\simeq 5\%$) fabrication error can lead to big differences in the drying pattern, the clearest example being figure 3.1.1c, where the drying front in a sample coming from the same master invades one side of the cell over the other due to such a manufacturing

error.

Regardless of this manufacturing noise, we are able to reproduce patterns well, as I show in figures 3.7 and ??, where we get a typical match of 60-70% or higher at breakthrough compared to the 90% or higher I find when repeating the same experiment. That means that even within the same design there is up to a 10% mismatch in the pattern. Furthermore, I have shown how, given the manufacturing tolerance in my experiments, the highest achievable match in the leading patterns is 70-80%. We do reach such a match in most patterns at breakthrough, making our result excellent, and I show that, in the cases where this threshold is not reached, manufacturing errors can be responsible for a very different evolution of the drying front into the porous medium.

4.1.3 Relative drying rates

The experiments were able to capture a three-dimensional effect – the constant and falling rate period [16, 20, 21]– that two dimensional models do not capture in the absence of film flow [87]. Experimental drying rates shown in this paper are often constant throughout the duration of experiments, although we did observe a few instances where the onset of a falling rate period was visible. The formation and persistence of isolated liquid clusters within the dry area alters the vapor concentration in the porous medium, supporting a faster drying rate than that predicted by the theory. On the other hand, simulations do not reproduce this trend, slowing down their drying rate early as evaporation occurs at the pore-space surface until the loss of surface wetness. Then, vapor diffusion within the medium is the dominant mechanism by which fluid is removed [20, 21], the drying front is still relatively close to the diffusive boundary, stabilizing the evaporation rate briefly. Isolated liquid clusters tend to evaporate at a higher rate in simulation than in

4 Discussion

experiments. This causes the drying front to effectively recede deeper into the medium causing the drying rates to drop again due to the relative lower efficiency of vapor diffusion as a fluid-removing mechanism.

4.1.4 Isolated liquid clusters

A discrepancy between experiments and simulations is the number of isolated liquid clusters in the dry area. I have already explained how the persistence of these clusters in the experiments influences drying rates. I have tried to investigate why these clusters do not evaporate as quickly as they do in the simulations. I tested the possibility of wettability effects not included in the model by repeating experiments where the cells were filled with water instead of oil, changing the contact angle of the liquid from $\sim 0^\circ$ to $\sim 70^\circ$. The resulting drying rate and leading patterns were not to be distinguished by the same experiment with oil. The only obvious difference was in the number of clusters formed. Water did not break down into as many isolated clusters due to its higher surface tension. However we see how isolated clusters still tend to evaporate slowly since the Euler number in Fig. 3.12, even though not as fast, keeps dropping as opposed to the trend shown by the corresponding simulations in Fig. 3.6 where the Euler number increases at later stages. That means that clusters evaporate at a higher rate than that at which they form.

The lower wettability of water did not change the leading pattern or the relative drying rate of the experiment. A higher contact angle inhibits the formation of films and gutter flows that may otherwise enhance liquid transport within the porous medium even showing a falling rate period in a two-dimensional model [87]. In the wettability range explored, inhibiting this mechanism only changed the number of clusters formed,

4.1 *Drying experiments*

but not the evaporation rate or leading pattern of the experiment showing that, if gutter and film flows were present in the experiments with oil, they would play a negligible role in the fluid transport. Besides this, the observation of a comparable relative drying rate despite the different numbers of isolated clusters suggests the density of clusters does not influence the drying rate. Rather, their position does. This statement is confirmed by the plots in Fig. 3.11. There, the drying rates were computed by taking an experimental pattern and estimating the drying rate at the next time step. This procedure allows a much closer estimation of experimental rates by the model, proving the importance of the pattern on the drying rate.

Another possible mechanism by which clusters may form is the presence of a non-volatile dissolved phase in the oil I have used for my experiments. This is unlikely, as Novec 7500 is engineered to be inert and finding a nonvolatile compound to dissolve in it was difficult. To test this possibility however, I have carried out a couple of experiments with water saturated with sodium carbonate. The results have shown how this non volatile phase changes the invasion pattern by forcing the drying front to explore areas of the chip that were not otherwise invaded in experiments with pure fluids. This result can be explained by considering precipitation of the salt at the larger pores, where evaporation preferentially occurs. Clogging these pores only leaves liquid with lower concentrations of salt to evaporate at the remaining available pores. Furthermore, the number of isolated clusters formed in these experiments was comparable to that of the same cells when using pure liquids. These observations allow me to conclude that the fluids I have used were indeed free of nonvolatile contaminants and that these possible contaminants would explain neither the formation nor the persistence of isolated liquid clusters.

4.1.5 Disorder effects

Random disorder does not show a clear effect on the metrics we have used to characterize our experiments in this paper, e.g faster drying rates for higher disorder. Simulations did not show a trend either although averaging over many realizations would be necessary to say something conclusive on this matter. We do not observe such trends and we have explained why, for lower amounts of disorder, this expectation is unreal: the manufacturing random error in the chips is too large for the actual disorder to emerge as a parameter determining differences. However, simulations do not carry such a systematic error and yet seeing a trend in single realizations is a hard task. One reason is that trends should be extracted from many randomizations, in order to have averages and reduce the error bars on the curves we plot. Doing this experimentally would be costly while computationally results can be produced in a matter of days. Such a test has been run by Oshri Borgman on samples with correlated disorder in [88], showing how increasing correlation length maintains the surface of the pore space wet for longer periods of times, enhancing transport and, consequently, drying rates. This result proves how the simulations can be used to extract results with higher efficiency than it is allowed by experiments.

Size-dependent drying rates in samples with correlated disorder are an interesting result. We do see in figure 3.8 how large pores are invaded first and contribute to most of the total drying rates. It is also interesting to see how the drying rates of large and small pores alternate their high and lows in bursts. This suggests the drying front invades all of the large pores made available by the liquid-vapor interface first. When only small pores are available, there is an invasion of these until a new patch of large pores is available, slowing down the small-pore drying rate again. This is a good result as it proves the assumption of the model, in which large pores should be invaded at a higher rate, is

correct. Further analysis on this bursting behavior is being performed statistically by Soumyajyoti Biswas and will be published in the future.

4.2 Displacement experiments

Experiments on fluid-fluid displacement are just beyond the proof-of-principle phase. I have not studied this phenomenon systematically but I have manufactured the samples and made a first experimental trial to prove the method established in the drying experiments can be extended to other systems. With this in mind, I will discuss the results I have achieved and compare them to the literature that motivated the experiments.

If we look at the phase plot in figure 3.14, we can see how more heterogeneous samples tend to show higher roughness in the final patterns. If we compare to the simulated phase plot we show in figure 3.14b it is obvious we do not see the fingering shown, even at the higher capillary numbers. However, if we compare to the experimental phase plot shown in figure 3.14c we achieve a higher resemblance even though I have worked at a smaller length-scale and I was able to manage a better control on the geometry of my samples. The experimental procedure we have used is somewhat different than that used in [25]. There, air was expanding freely into the sample as the liquid was being sucked to the outside (constant pressure), while in our experiments air was injected in the middle of the pore-space, enforcing a constant injection rate. The latter procedure introduces a parameter that is otherwise absent in the model: compressibility of the invading phase. A compressible fluid could not be added trivially to the model and it is most likely responsible for the discrepancy observed.

4 Discussion

I have discussed the reasons for the differences between model and experiments. I would now like to discuss the results these experiments have produced. Once again, I had four samples of which three had the same relative disorder –these samples were scaled to increase or decrease the size of single pillars while maintaining the same average size– and one was randomized to have 20% heterogeneity again, but with a different seed. From figure 3.2 we can observe a trend. Of course the statistics here are not strong enough to make a final statement, but a trend depending on the level of heterogeneity in the samples is visible. Higher disorder seems to lead to lower residual saturations in the pore-space and lower α , namely, a rougher pattern. The trend is not as obvious when looking at the number of isolated fluid clusters, but we do typically observe more isolated clusters at higher disorders through the capillary number interval investigated. A further proof of what we are stating is given by the two realizations of a sample with 20% heterogeneity. When re-randomizing the geometry of a cell, we obtain different results in the single metrics, but it is interesting to observe how the two samples with 20% disorder tend to lie between the extreme cases of high (37%) and low (3%) disorder. I want to remark that more experiments are needed to make this a final statement, but it is likely that, with better statistics, this trend could be confirmed.

For the purpose of this thesis, I wanted to show that microfluidic cells could be employed to study two-phase flow in granular materials. Comparisons to models and similar experiments have shown how drying and two-fluid displacement could be studied using such microfluidic chips, although salt transport and deposition and pore-elasticity are two immediate applications that have been started in our group by Wieland Lühder and by Benjamin Dimond in his Bachelor’s thesis [89].

5 Conclusion and Outlook

I have made quasi-two-dimensional granular materials using microfluidic techniques [74, 70, 72]. The grains were made by round pillars of controlled, heterogeneous sizes. Pillar-size disorder was introduced by imposing either a random uniform distribution or a correlated, Gaussian distribution clipped to avoid overlaps. Two kinds of phenomena were studied: drying in granular materials and immiscible fluid-fluid displacement.

I have shown how microfluidic cells can be a valid two-dimensional micromodel to study flows in granular materials. The strength of this method lies in the control it allows over the geometry of the samples, improving on analogous experiments using glass beads [13, 67]. Comparing to previous experiments on two-dimensional micromodels [54, 64, 65], my method allows to reduce throats to one dimensional objects controlling the communication between pores, as would be the case in real three-dimensional granular packings. A further point that was improved upon using microfluidic cells was the ability of reaching soil-scale, which was not yet achieved by similar previous experiments [25, 45, 66, 68].

The particles in my samples were placed on a square or a triangular grid, allowing control over the possible pore invasion mechanisms. Specifically, in drying experiments I have used a square grid, where bursts are the only pore-invasion mode allowed, while

5 Conclusion and Outlook

in displacement experiments we have used a triangular grid that also allows touch and overlap as further invasion modes.

In the case of drying experiments I was able to capture a typically three-dimensional effect such as the falling rate period. In two dimensional simulations, this constant rate/falling rate period is never observed in the absence of film flows that support a higher, constant drying rate in the earlier stages of drying [87], while in three-dimensional simulations the constant rate is a consequence of the liquid chimneys connecting the bulk of the fluid to the surface of the porous medium for a longer time [21, 16]. I did show how the pattern influences the drying rates. In fact, the higher number and longer persistence of isolated clusters of fluid in the experiments enhances vapor diffusion, supporting a higher drying rate than predicted by the model, where these clusters evaporate quickly, reducing the vapor concentration close to the pore-space surface. The difference in vapor concentration seems to be enough for the experimental drying rates to stay higher for a longer period of time.

Together with our colleagues in Israel, we have estimated how well the model can capture experimental patterns, neglecting the difference in isolated liquid clusters, by comparing patterns pore-by-pore. We have achieved a leading pattern match of 70-80% in the best cases. I actually show how the manufacturing tolerance in our samples would not allow a better match anyway, making our result excellent in that light.

In the case of immiscible fluid-fluid displacement I have shown it is possible to make these systems using microfluidic techniques. Comparing to experiments done before by other groups such as [25, 68], I was able to reach smaller scales once again, while maintaining the ability to explore a broad range of conditions.

When comparing to the model, I do not see the same fingering in the resulting patterns. This maybe due to effects of air compressibility that are not included in the model. However, if we compare to analogous experiments shown in [25], our results are very close in the Capillary number range explored. It is however noteworthy that in [25] the experimental procedure was slightly different. In fact, they had air expanding freely into the medium by sucking the fluid out of the extremities, rather than injecting air from the center of the cell. This different procedure removes the problem of including air compressibility in the model, which is planned. I was also limited in the capillary number range I could explore, since my syringe pump did not allow reaching capillary numbers higher than 10^{-3} . Despite the different experimental conditions, I was still able to see a trend in the behavior of our cells, with more heterogeneous samples giving rougher fronts than their ordered counterparts, which is the thesis tested in [25]. This shows my cells are also suitable to study other phenomena in porous media flow.

There are further tests that would make the experiments presented so far more complete. For example larger cells could be fabricated in order to reduce finite size effects and to test the effects of gravity over a drying front. Gravity can also play a role in three-dimensional packings and, in the two-dimensional experiments presented so far, gravity was excluded completely.

To increase the system's complexity while maintaining the simplicity of dealing with two dimensions, the round pillars could be made into polygons. Corners in the shape of particles are known to trigger pinning of fluid-fluid interfaces. Furthermore, we are not restricted by convex polygons, as natural soils and rocks are not, and could realize a slice of real soil to gain insights on multiphase flow in porous media.

5 Conclusion and Outlook

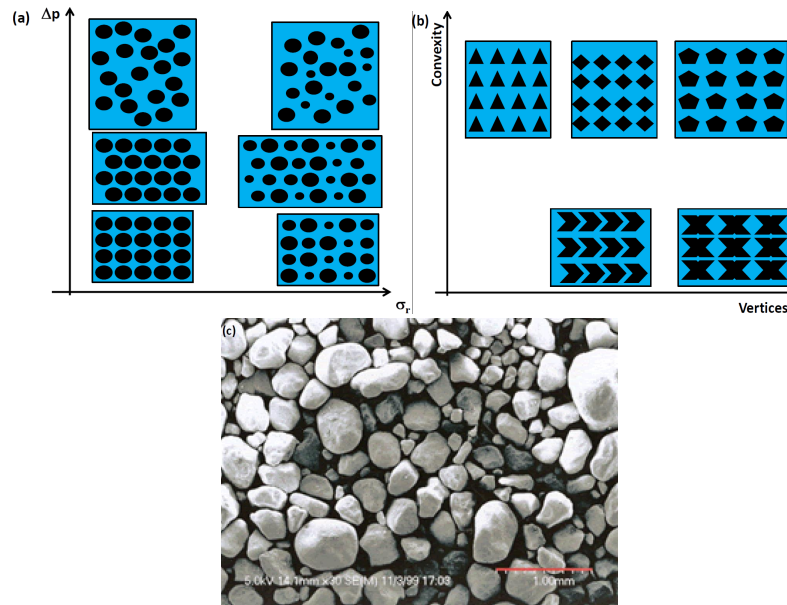


Figure 5.1: Different achievable levels of disorder. (a) We can change the size heterogeneity of particles, their position or both at the same time. In order to make the samples more and more similar to real, random granular packings (b) we can also change the shapes and convexity of the particles. The goal is to achieve complexity (c) one would have when taking a 'slice' of real soil while allowing application of the simpler realization and analysis tools that are available when working in quasi-two-dimensional systems.

We are not restricted to a grid either and could make random packings of randomly-sized and shaped pillars. This would be the most real setting achievable while maintaining two-dimensional geometries allowing to extend the techniques established in this thesis to applications to processes like oil recovery or, for example, drying of foods.

Following on the work of [89] it would be possible to apply the cells I have made for this thesis to the study of deformable granular media, with pore volumes depending also on the pressure of the fluid. In order to do that, one would need to change the experimental

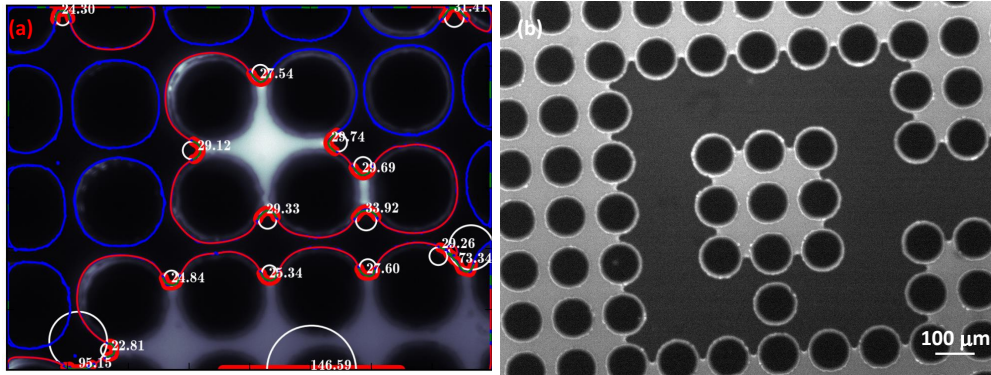


Figure 5.2: Possible further investigations on the medium’s elasticity and film flow. I show a microscope picture of a sample where I tracked the air-liquid interface curvature (a) to determine the pressure in the fluid and, consequently, understand how the clusters communicate (work of Dr. Daniel Herde). In (b) I show how introducing defects in the samples can be a tool to study the importance of film flow within porous media.

resolution by observing the samples with a microscope and the material of which the chip is made in order to have an elastic matrix. For example, PDMS would be a good substitute for NOA in the drying experiments for this test. One would then be able to track pillar deformations and study the effects introduced by having a deformable cell. This was introduced as a proof of principle experiment developed in our group ([89]), showing that tracking of such deformations is possible.

In order to study the importance of film flow and, possibly, understand the formation and persistence of isolated liquid clusters, one can use microscope pictures of our samples to track air-liquid interfaces and, consequently, the pressure in the fluid by use of Laplace’s equation. If far clusters were to show the same pressure, that would mean they are still connected in some way, possibly by hard-to-track films. Otherwise, independent evolution of liquid pressures in isolated clusters would prove the absence of such films.

5 *Conclusion and Outlook*

An example of this method is shown in Fig. 4.2. There, we show a PDMS sample filled with dyed water where we have estimated the curvature of air-water menisci (units are in pixels –work of Dr. Daniel Herde). Because of the limited field of view, we could promote the formation of isolated liquid clusters by introducing ‘defects’ in the samples, e.g. Fig. 4.2b. Configurations like that shown force the formation of isolated clusters whose pressure we can track to determine their connectivity to apparently non-connected clusters of fluid.

The possibilities I have discussed so far are only the first that come to mind when dealing with such systems. The message I would like to give is that cells like the ones I have used in my work can be tuned at will to study multiphase flow in granular materials in a simple way. Compared to analogous three-dimensional experiments, two-dimensional cells allow a greater degree of control over the geometry of the samples and simpler optical analysis tools. Furthermore, modelling methods are more efficient in two dimensions, as opposed to the limited numerical resolution and experimental complications that are necessary to study the same phenomena in three dimensions. These restrictions make two-dimensional microfluidic models a practical method of investigation on multiphase flow in granular materials.

Acknowledgements

I would like to thank first of all my supervisor, Lucas Goehring, for guiding me and helping me in my work at the Max Planck Institute.

Ran Holtzman and Oshri Borgman, my collaborators in Israel, for providing the simulations to compare with my experiments.

Wieland Lühder for the contribution to the image analysis. That was a serious breakthrough in my project and allowed comparing experiments and simulations in an unprecedented way.

Although I have not eventually used his contributions directly in my thesis, I would like to thank Daniel Herde who helped advancing my project beyond its first sticking point.

Ralf Seemann and his student, Michael Jung, for the advice. They have helped beyond a second sticking point in my work.

Finally, I would like to thank the Max Planck Institute for supporting me in my research and all the people that have accompanied me throughout my stay. Especially Barbara Kutz, who helped me way beyond her job description.

I did the rest.

5 *Conclusion and Outlook*

Bibliography

- [1] D. Nielsen, J. Biggar, *et al.*, “Water flow and solute transport processes in the unsaturated zone,” *Water Resour. Res.*, vol. 22, no. 9S, 1986.
- [2] R. Holtzman and R. Juanes, “Thermodynamic and hydrodynamic constraints on overpressure caused by hydrate dissociation: A pore-scale model,” *Geophys. Res. Lett.*, vol. 38, no. 14, p. L14308, 2011.
- [3] S. Berg, H. Ott, S. a. Klapp, A. Schwing, R. Neiteler, N. Brussee, A. Makurat, L. Leu, F. Enzmann, J.-O. Schwarz, M. Kersten, S. Irvine, and M. Stampanoni, “Real-time 3D imaging of Haines jumps in porous media flow.,” *Proceedings of the National Academy of Sciences of the United States of America*, no. 14, 2013.
- [4] J. M. Nordbotten, M. A. Celia, and S. Bachu, “Injection and storage of co2 in deep saline aquifers: Analytical solution for co2 plume evolution during injection,” *Transport in Porous media*, vol. 58, no. 3, pp. 339–360, 2005.
- [5] U. Nachshon, N. Weisbrod, M. I. Dragila, and A. Grader, “Combined evaporation and salt precipitation in homogeneous and heterogeneous porous media,” *Water Resour. Res.*, vol. 47, no. 3, p. W03513, 2011.
- [6] M. N. Rad, N. Shokri, and M. Sahimi, “Pore-scale dynamics of salt precipitation in drying porous media,” *Phys. Rev. E*, vol. 88, no. 3, p. 032404, 2013.

Bibliography

- [7] F. Nadim, G. E. Hoag, S. Liu, R. J. Carley, and P. Zack, “Detection and remediation of soil and aquifer systems contaminated with petroleum products: an overview,” *J. Petrol. Sci. Eng.*, vol. 26, no. 1, pp. 169–178, 2000.
- [8] R. Toussaint, K. Må løy, Y. Méheust, G. Lø voll, M. Jankov, G. Schäfer, and J. Schmittbuhl, “Two-phase flow: structure, upscaling, and consequences for macroscopic transport properties,” *Vadose Zone Journal*, vol. 11, no. 3, 2012.
- [9] R. T. Armstrong and S. Berg, “Interfacial velocities and capillary pressure gradients during haines jumps,” *Phys. Rev. E*, vol. 88, no. 4, p. 043010, 2013.
- [10] P. Lehmann, S. Assouline, and D. Or, “Characteristic lengths affecting evaporative drying of porous media,” *Phys. Rev. E*, vol. 77, no. 5, p. 056309, 2008.
- [11] J. R. Philip, “Evaporation, and moisture and heat fields in the soil,” *J. Meteor.*, vol. 14, no. 4, pp. 354–366, 1957.
- [12] L. Bernstein, “Effects of salinity and sodicity on plant growth,” *Annu. Rev. Phytopathol.*, vol. 13, no. 1, pp. 295–312, 1975.
- [13] T. Shaw, “Drying as an immiscible displacement process with fluid counterflow,” *Phys. Rev. Lett.*, vol. 59, no. 15, p. 1671, 1987.
- [14] W. B. Haines, “Studies in the physical properties of soil. v. the hysteresis effect in capillary properties, and the modes of moisture distribution associated therewith,” *J. Agric. Sci.*, vol. 20, no. 01, pp. 97–116, 1930.
- [15] L. Xu, S. Davies, A. B. Schofield, and D. A. Weitz, “Dynamics of drying in 3d porous media,” *Phys. Rev. Lett.*, vol. 101, no. 9, p. 094502, 2008.

- [16] N. Shokri, P. Lehmann, and D. Or, “Liquid-phase continuity and solute concentration dynamics during evaporation from porous media: Pore-scale processes near vaporization surface,” *Phys. Rev. E*, vol. 81, no. 4, p. 046308, 2010.
- [17] E. Shahraeeni, P. Lehmann, and D. Or, “Coupling of evaporative fluxes from drying porous surfaces with air boundary layer: Characteristics of evaporation from discrete pores,” *Water Resour. Res.*, vol. 48, no. 9, p. W09525, 2012.
- [18] M. Suzuki and S. Maeda, “On the mechanism of drying of granular beds,” *J. Chem. Eng. Jpn.*, vol. 1, no. 1, pp. 26–31, 1968.
- [19] P. Lehmann and D. Or, “Effect of wetness patchiness on evaporation dynamics from drying porous surfaces,” *Water Resour. Res.*, vol. 49, no. 12, pp. 8250–8262, 2013.
- [20] F. Chauvet, P. Duru, S. Geoffroy, and M. Prat, “Three periods of drying of a single square capillary tube,” *Phys. Rev. Lett.*, vol. 103, no. 12, p. 124502, 2009.
- [21] N. Shokri and D. Or, “What determines drying rates at the onset of diffusion controlled stage-2 evaporation from porous media?,” *Water Resour. Res.*, vol. 47, no. 9, p. W09513, 2011.
- [22] F. Orr and J. Taber, “Use of carbon dioxide in enhanced oil recovery,” *Science*, vol. 224, no. 4649, pp. 563–569, 1984.
- [23] M. Sahimi, *Flow and transport in porous media and fractured rock: from classical methods to modern approaches*. John Wiley & Sons, 2011.
- [24] L. Cueto-Felgueroso and R. Juanes, “Nonlocal interface dynamics and pattern formation in gravity-driven unsaturated flow through porous media,” *Physical Review Letters*, vol. 101, no. 24, p. 244504, 2008.

Bibliography

- [25] R. Holtzman, “Effects of pore-scale disorder on fluid displacement in partially-wettable porous media,” *Scientific Reports*, vol. 6, p. 6:36221, 2016.
- [26] R. Holtzman and E. Segre, “Wettability stabilizes fluid invasion into porous media via nonlocal, cooperative pore filling,” *Phys. Rev. Lett.*, vol. 115, no. 16, p. 164501, 2015.
- [27] M. Jung, M. Brinkmann, R. Seemann, T. Hiller, M. S. de La Lama, and S. Herminghaus, “Wettability controls slow immiscible displacement through local interfacial instabilities,” *Physical Review Fluids*, vol. 1, no. 7, p. 074202, 2016.
- [28] M. Alava, M. Dubé, and M. Rost, “Imbibition in disordered media,” *Adv. Phys.*, vol. 53, no. 2, pp. 83–175, 2004.
- [29] P. Pelcé, *New visions on form and growth: fingered growth, dendrites, and flames*. Oxford University Press on Demand, 2004.
- [30] H. Ji and M. O. Robbins, “Transition from compact to self-similar growth in disordered systems: Fluid invasion and magnetic-domain growth,” *Phys. Rev. A*, vol. 44, no. 4, p. 2538, 1991.
- [31] T. Bultreys, W. De Boever, and V. Cnudde, “Imaging and image-based fluid transport modeling at the pore scale in geological materials: A practical introduction to the current state-of-the-art,” *Earth-Science Rev.*, vol. 155, pp. 93–128, 2016.
- [32] H. A. Stone, A. D. Stroock, and A. Ajdari, “Engineering flows in small devices: microfluidics toward a lab-on-a-chip,” *Annu. Rev. Fluid Mech.*, vol. 36, pp. 381–411, 2004.
- [33] H. Kim, Z. Zheng, and H. A. Stone, “Noncircular stable displacement patterns in a meshed porous layer,” *Langmuir*, vol. 31, no. 20, pp. 5684–5688, 2015.

- [34] J. M. Matter, M. Stute, S. Ó. Snæbjörnsdóttir, E. H. Oelkers, S. R. Gislason, E. S. Aradóttir, B. Sigfusson, I. Gunnarsson, H. Sigurdardóttir, E. Gunnlaugsson, *et al.*, “Rapid carbon mineralization for permanent disposal of anthropogenic carbon dioxide emissions,” *Science*, vol. 352, no. 6291, pp. 1312–1314, 2016.
- [35] L. W. Lake, R. Johns, W. Rossen, and G. Pope, *Fundamentals of enhanced oil recovery*. Society of Petroleum Engineers, 1986.
- [36] Y. C. Yortsos, B. Xu, and D. Salin, “Phase diagram of fully developed drainage in porous media,” *Phys. Rev. Lett.*, vol. 79, no. 23, p. 4581, 1997.
- [37] M. Cieplak and M. O. Robbins, “Dynamical transition in quasistatic fluid invasion in porous media,” *Phys. Rev. Lett.*, vol. 60, no. 20, p. 2042, 1988.
- [38] M. Cieplak and M. O. Robbins, “Influence of contact angle on quasistatic fluid invasion of porous media,” *Phys. Rev. B*, vol. 41, no. 16, p. 11508, 1990.
- [39] R. Toussaint, G. Løvoll, Y. Méheust, K. J. Måløy, and J. Schmittbuhl, “Influence of pore-scale disorder on viscous fingering during drainage,” *EPL (Europhysics Letters)*, vol. 71, no. 4, p. 583, 2005.
- [40] R. Holtzman and R. Juanes, “Crossover from fingering to fracturing in deformable disordered media,” *Phys. Rev. E*, vol. 82, no. 4, p. 046305, 2010.
- [41] W. Xu, J. T. Ok, F. Xiao, K. B. Neeves, and X. Yin, “Effect of pore geometry and interfacial tension on water-oil displacement efficiency in oil-wet microfluidic porous media analogs,” *Phys. Fluids (1994-present)*, vol. 26, no. 9, p. 093102, 2014.
- [42] H. Liu, Y. Zhang, and A. J. Valocchi, “Lattice boltzmann simulation of immiscible fluid displacement in porous media: Homogeneous versus heterogeneous pore network,” *Phys. Fluids (1994-present)*, vol. 27, no. 5, p. 052103, 2015.

Bibliography

- [43] N. Martys, M. O. Robbins, and M. Cieplak, “Scaling relations for interface motion through disordered media: Application to two-dimensional fluid invasion,” *Phys. Rev. B*, vol. 44, no. 22, p. 12294, 1991.
- [44] J.-D. Chen and D. Wilkinson, “Pore-scale viscous fingering in porous media,” *Phys. Rev. Lett.*, vol. 55, no. 18, p. 1892, 1985.
- [45] A. Ferrari, J. Jimenez-Martinez, T. L. Borgne, Y. Méheust, and I. Lunati, “Challenges in modeling unstable two-phase flow experiments in porous micromodels,” *Water Resour. Res.*, vol. 51, no. 3, pp. 1381–1400, 2015.
- [46] R. Holtzman and R. Juanes, “Crossover from fingering to fracturing in deformable disordered media,” *Physical Review E*, vol. 82, no. 4, 2010.
- [47] I. Fatt, “The network model of porous media,” *Petrol. Trans. AIME*, vol. 207, pp. 144–181, 1956.
- [48] M. J. Blunt, M. D. Jackson, M. Piri, and P. H. Valvatne, “Detailed physics, predictive capabilities and macroscopic consequences for pore-network models of multiphase flow,” *Adv. Water Resour.*, vol. 25, no. 8, pp. 1069–1089, 2002.
- [49] A. G. Yiotis, A. K. Stubos, A. G. Boudouvis, and Y. C. Yortsos, “A 2-D pore-network model of the drying of single-component liquids in porous media,” *Adv. Water Resour.*, vol. 24, no. 3-4, pp. 439–460, 2001.
- [50] M. Prat, “Percolation model of drying under isothermal conditions in porous media,” *Int. J. Multiphase Flow*, vol. 19, no. 4, pp. 691–704, 1993.
- [51] S. Nowicki, H. Davis, and L. Scriven, “Microscopic determination of transport parameters in drying porous media,” *Dry. Technol.*, vol. 10, no. 4, pp. 925–946, 1992.

- [52] I. Tsimpanogiannis, Y. Yortsos, S. Poulou, N. Kanellopoulos, and A. Stubos, “Scaling theory of drying in porous media,” *Phys. Rev. E*, vol. 59, no. 4, p. 4353, 1999.
- [53] A. G. Yiotis, A. G. Boudouvis, A. K. Stubos, I. N. Tsimpanogiannis, and Y. C. Yortsos, “Effect of liquid films on the drying of porous media,” *AIChE Journal*, vol. 50, no. 11, pp. 2721–2737, 2004.
- [54] J. Laurindo and M. Prat, “Numerical and experimental network study of evaporation in capillary porous media. Drying rates,” *Chem. Eng. Sci.*, vol. 53, no. 12, pp. 2257–2269, 1998.
- [55] R. Lenormand, “Liquids in porous media,” *J. Phys. Condens. Matter*, vol. 2, no. S, p. SA79, 1990.
- [56] R. Lenormand, E. Touboul, and C. Zarcone, “Numerical models and experiments on immiscible displacements in porous media,” *J. Fluid Mech.*, vol. 189, pp. 165–187, 1988.
- [57] C. Cottin, H. Bodiguel, and A. Colin, “Influence of wetting conditions on drainage in porous media: A microfluidic study,” *Phys. Rev. E*, vol. 84, no. 2, p. 026311, 2011.
- [58] N. Shahidzadeh-Bonn, A. Tournié, S. Bichon, P. Vié, S. Rodts, P. Faure, F. Bertrand, and A. Azouni, “Effect of wetting on the dynamics of drainage in porous media,” *Transp. Porous Media*, vol. 56, no. 2, pp. 209–224, 2004.
- [59] S. He, G. L. Kahanda, and P.-z. Wong, “Roughness of wetting fluid invasion fronts in porous media,” *Phys. Rev. Lett.*, vol. 69, no. 26, p. 3731, 1992.
- [60] J. Stokes, D. Weitz, J. P. Gollub, A. Dougherty, M. Robbins, P. Chaikin, and

Bibliography

- H. Lindsay, “Interfacial stability of immiscible displacement in a porous medium,” *Phys. Rev. Lett.*, vol. 57, no. 14, p. 1718, 1986.
- [61] R. Rangel and S. Rojas, “Montecarlo dla-type simulations of wetting effects in fluid displacement in porous media,” *Comput. Geosci.*, vol. 13, no. 2, pp. 215–225, 2009.
- [62] H. Liu, A. J. Valocchi, Q. Kang, and C. Werth, “Pore-scale simulations of gas displacing liquid in a homogeneous pore network using the lattice boltzmann method,” *Transp. Porous Media*, vol. 99, no. 3, pp. 555–580, 2013.
- [63] M. Trojer, M. L. Szulczewski, and R. Juanes, “Stabilizing fluid-fluid displacements in porous media through wettability alteration,” *Phys. Rev. Applied*, vol. 3, no. 5, p. 054008, 2015.
- [64] N. Vorhauer, T. Metzger, E. Tsotsas, and M. Prat, “Experimental investigation of drying by pore networks: influence of pore size distribution and temperature,” *In: 4th International Conference on Porous Media and its Applications in Science, Engineering and Industry*, June 2012.
- [65] N. Vorhauer, Y. Wang, A. Kharaghani, E. Tsotsas, and M. Prat, “Drying with formation of capillary rings in a model porous medium,” *Transport Porous Med.*, vol. 110, no. 2, pp. 197–223, 2015.
- [66] O. Aursjø, G. Løvoll, H. A. Knudsen, E. G. Flekkøy, and K. J. Måløy, “A direct comparison between a slow pore scale drainage experiment and a 2d lattice boltzmann simulation,” *Transport Porous Med.*, vol. 86, no. 1, pp. 125–134, 2011.
- [67] E. Aker, K. J. Måløy, A. Hansen, and S. Basak, “Burst dynamics during drainage displacements in porous media: Simulations and experiments,” *Europhys. Lett.*, vol. 51, no. 1, p. 55, 2000.

- [68] B. Zhao, C. W. MacMinn, and R. Juanes, “Wettability control on multiphase flow in patterned microfluidics,” *Proc. Nat. Acad. Sci.*, vol. 113, no. 37, pp. 10251–10256, 2016.
- [69] K. Pillai, M. Prat, and M. Marcoux, “A study on slow evaporation of liquids in a dual-porosity porous medium using square network model,” *Int. J. Heat Mass Tran.*, vol. 52, no. 7, pp. 1643–1656, 2009.
- [70] G. M. Whitesides, “The origins and the future of microfluidics,” *Nature*, vol. 442, no. 7101, pp. 368–373, 2006.
- [71] A. D. Stroock and G. M. Whitesides, “Components for integrated poly (dimethylsiloxane) microfluidic systems,” *Electrophoresis*, vol. 23, no. 20, pp. 3461–3473, 2002.
- [72] G. M. Whitesides and A. D. Stroock, “Flexible methods for microfluidics,” *Phys. Today*, vol. 54, no. 6, pp. 42–48, 2001.
- [73] Y. Xia and G. M. Whitesides, “Soft lithography,” *Ann. rev. mat. sci.*, vol. 28, no. 1, pp. 153–184, 1998.
- [74] M. J. Madou, *Fundamentals of microfabrication: the science of miniaturization*. CRC press, 2002.
- [75] R. J. Jackman, J. L. Wilbur, and G. M. Whitesides, “Fabrication of submicrometer features on curved substrates by microcontact printing,” *Science*, vol. 269, no. 5224, p. 664, 1995.
- [76] Shipley, *Microposit s1800 series photoresist*. <http://engineering.dartmouth.edu/microeng/processing/lithography/S1800>
- [77] Kayakumicrochem, *SU8 Negative tone photoresist formulations 50 - 100*.

Bibliography

- [78] Kayakumicrochem, *SU8 3000 permanent epoxy negative photoresist*.
<http://www.microchem.com/pdf/SU-8>
- [79] L. Zhang, H. Chen, J. Sun, and J. Shen, "Layer-by-layer deposition of poly (di-allyldimethylammonium chloride) and sodium silicate multilayers on silica-sphere-coated substrate-facile method to prepare a superhydrophobic surface," *Chemistry of materials*, vol. 19, no. 4, pp. 948–953, 2007.
- [80] S. Silvestrini, D. Ferraro, T. Tóth, M. Pierno, T. Carofiglio, G. Mistura, and M. Maggini, "Tailoring the wetting properties of thiolene microfluidic materials," *Lab on a Chip*, vol. 12, no. 20, pp. 4041–4043, 2012.
- [81] S. Bhattacharya, A. Datta, J. M. Berg, and S. Gangopadhyay, "Studies on surface wettability of poly (dimethyl) siloxane (pdms) and glass under oxygen-plasma treatment and correlation with bond strength," *Journal of microelectromechanical systems*, vol. 14, no. 3, pp. 590–597, 2005.
- [82] W. Lühder, "Influence of pore-size heterogeneity on the drying processes in porous materials," 2015. BSc. Thesis Georg-August-Universität, Göttingen, 2015.
- [83] K. Mecke, "Morphological characterization of patterns in reaction-diffusion systems," *Phys. Rev. E*, vol. 53, no. 5, p. 4794, 1996.
- [84] K. Mecke and C. Arns, "Fluids in porous media: a morphometric approach," *J. Phys.-Condensed Mat.*, vol. 17, no. 9, p. S503, 2005.
- [85] J. Becker, G. Grün, R. Seemann, H. Mantz, K. Jacobs, K. R. Mecke, and R. Blossey, "Complex dewetting scenarios captured by thin-film models," *Nat. Mat.*, vol. 2, no. 1, pp. 59–63, 2003.

- [86] P. Meakin and A. M. Tartakovsky, “Modeling and simulation of pore-scale multi-phase fluid flow and reactive transport in fractured and porous media,” *Rev. Geophys.*, vol. 47, no. 3, 2009.
- [87] M. Prat, “On the influence of pore shape, contact angle and film flows on drying of capillary porous media,” *Int. J. Heat Mass Trans.*, vol. 50, no. 7-8, pp. 1455–1468, 2007.
- [88] O. Borgman, P. Fantinel, W. Lühder, L. Goehring, and R. Holtzman, “Pore scale study of drying in spatially correlated porous media,” 2016. <http://arxiv.org/abs/1612.01032>.
- [89] B. Dimond, “Biogenic cracks in porous medium.” BSc. Thesis Georg-August-Universität, Göttingen, 2015.

Bibliography

Curriculum vitae

PAOLO FANTINEL

Vittorio Veneto(TV), Italy

Nationality: Italian

Education:

2007-2010 BSc. IN PHYSICS

Dissertation Title: FABRICATION OF SUPERHYDROPHOBIC SURFACES
WITH LITHOGRAPHIC TECHNIQUES

2010-2012 MSc. IN PHYSICS

Dissertation Title: SLIPPING OF DROPLETS ON GEOMETRICALLY
PATTERNED SURFACES

Publications:

STICK-SLIP SLIDING OF WATER DROPS ON CHEMICALLY HETEROGENEOUS
SURFACES, S. Varagnolo, D. Ferraro, P. Fantinel, M. Pierno, G. Mistura, G. Amati, L.
Biferale, and M. Sbraglia Phys. Rev. Lett. 111, 066101 Published 5 August 2013

VALIDATING PORE-SCALE MODELS OF DRYING USING MICROFLUIDIC EXPERIMENTS, P.
Fantinel, O. Borgman, R. Holtzman, and L. Goehring, Submitted to Physical Review
Fluids

IMPACT OF SPATIALLY CORRELATED PORE-SCALE HETEROGENEITY ON DRYING
POROUS MEDIA, O. Borgman, P. Fantinel, W. Lühder, L. Goehring, and R. Holtzman,
Submitted to Water Resources Research